Chapter 4- Result and discussions

Results and discussion of the present work have been divided into three sections.

- **Section 4.1:** Selection of suitable graphene oxide-based support for bismuth ferrite in photocatalytic degradation process.
- **Section 4.2:** Synergistic effect of N-rGO supported Gd-doped bismuth ferrite on photocatalytic degradation of Rhodamine B
- **Section 4.3:** Sono-photocatalytic degradation of Rhodamine B over N-rGO supported Gd-doped bismuth ferrite heterojunction.

4.1 Selection of suitable graphene oxide-based support for bismuth ferrite in photocatalytic degradation process

Nowadays, Graphene is the most popular material to form semiconductor /graphene composite to developed high-performance photocatalyst [204]. Various functional groups associated with graphene oxide chemically interact with semiconductors and serves electron transfer from the conduction band edge of semiconductor to graphene oxide. Also, owing to its large surface area and various attached functional groups, graphene provides adequate active sites for the adsorption of organic pollutants prompting improved photocatalytic activity [205].

However, despite the graphene has high electrical conductivity, high surface area, and ballistic charge transport, recombination of charge carriers in graphene-supported photocatalysts has not completely curbed in graphene. To overcome this, there is a need of a sharp increase in electrical conductivity of graphene. This could be achieved by doping heteroatom in graphene. Therefore, doping of heteroatoms into graphene oxide nanosheets has been widely investigated. Among different heteroatoms, nitrogen-doped graphene has been reported to effectively increase the electrical conductivity and thus facilitates a quick transfer of photoinduced electrons resulting in the increased performance of photocatalysts [206]. In this regard, nitrogen-doped graphene oxide (N-rGO) supported bismuth ferrite (BFO/N-rGO) was synthesized by the sol-gel method followed by hydrothermal method. Catalysts were characterized by X-ray photoelectron spectroscopy (XPS), Fourier transform-infrared (FT-IR), Diffused reflectance spectroscopy (DRS), Electrical impedance spectroscopy (EIS), Photoluminescence (PL), and Mott-Schottky (M-S) analyses. Photoluminescence (PL) spectroscopy confirmed that nitrogen-doped graphene efficiently inhibits recombination of electron-hole pairs. FTIR, DRS, and XPS analyses confirmed a chemical interaction between graphene and bismuth

ferrite leading to the formation of heterojunction. This interaction led to the enhancement of charge transfer for photocatalytic activity. EIS and M-S analyses showed resistance for charge mobility, charge carrier density, and band bending in the catalysts.

4.1.1 XRD studies

XRD patterns of the synthesized catalysts are shown in Fig. 4.1.1. After the reduction of GO, diffraction peak of (002) plane shifted from 2θ =11.5 to 24.3^0 with an interlayer distance of 0.77 and 0.37 nm, respectively. Reduction of the interplanar spacing due to the removal of oxygenated functional groups from GO affirms that graphene oxide reduced successfully [207]. Further, due to incorporation of the nitrogen atom into rGO, the characteristic peak (002) shifted toward $2\theta = 26.11^0$, which is closed to well-ordered graphitic nature because nitrogen has a smaller atomic radius (0.70 Å) than a carbon atom (0.77Å). The replacement of carbon atom from the lattice of graphene oxide by nitrogen atom would decrease the interplanar spacing. Diffraction peak was also observed at 2θ ~43^0 in GO, rGO, and N-rGO, which are attributed to graphene layer with regular spacing but different stacking orders, which is known as turbostratic band disorder.

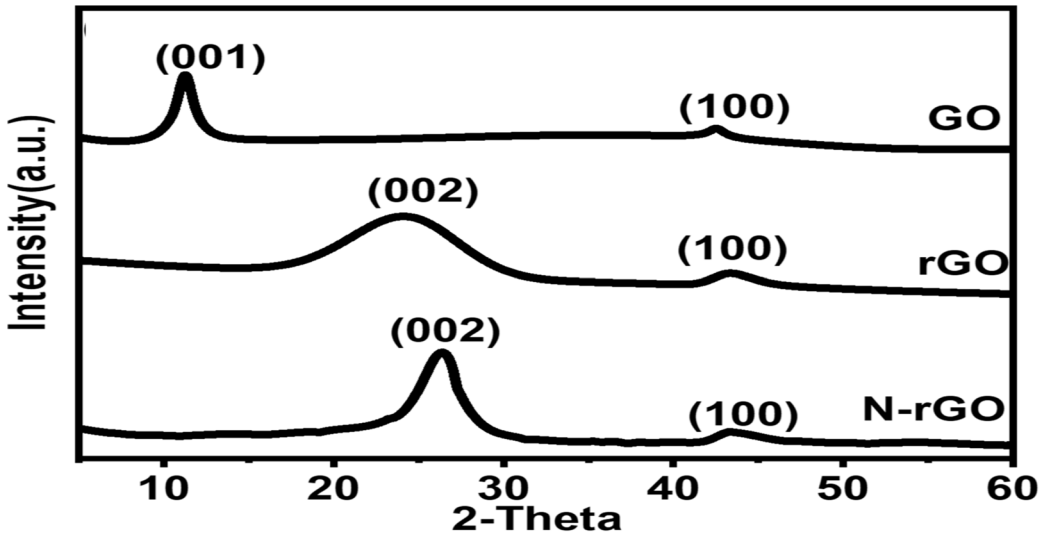

Fig. 4.1. 1 XRD patterns of GO, rGO, and N-rGO.

Diffraction peaks of BFO exhibited (012), (104), (110), (202), (024), (122), (018), and (214) planes which belong to rhombohedral perovskite phase of bismuth ferrite according to JCPDS PDF no 71-2494. Additional minor peaks were also observed, indicating the existence of some other phases such as $Bi_2Fe_4O_9$ and $Bi_{25}FeO_{40}$ according to JCPDS PDF no 74-1098 and 46-0416. Literature also reports the presence of other phases, along with perovskite $BiFeO_3$ [208]. It is noted that on the incorporation of rGO and N-rGO in BFO/rGO and BFO/N-rGO, respectively, planes (116) and (122) of BFO merge, and a broad peak appears at around $2\theta=51^0$, which shows the interaction between rGO/N-rGO and bismuth ferrite (the enlarged portion of Fig. 4.1.2). Average crystallite size for all the catalysts were calculated and given in Table 4.1.2. A similar observation has been described in earlier research [209].

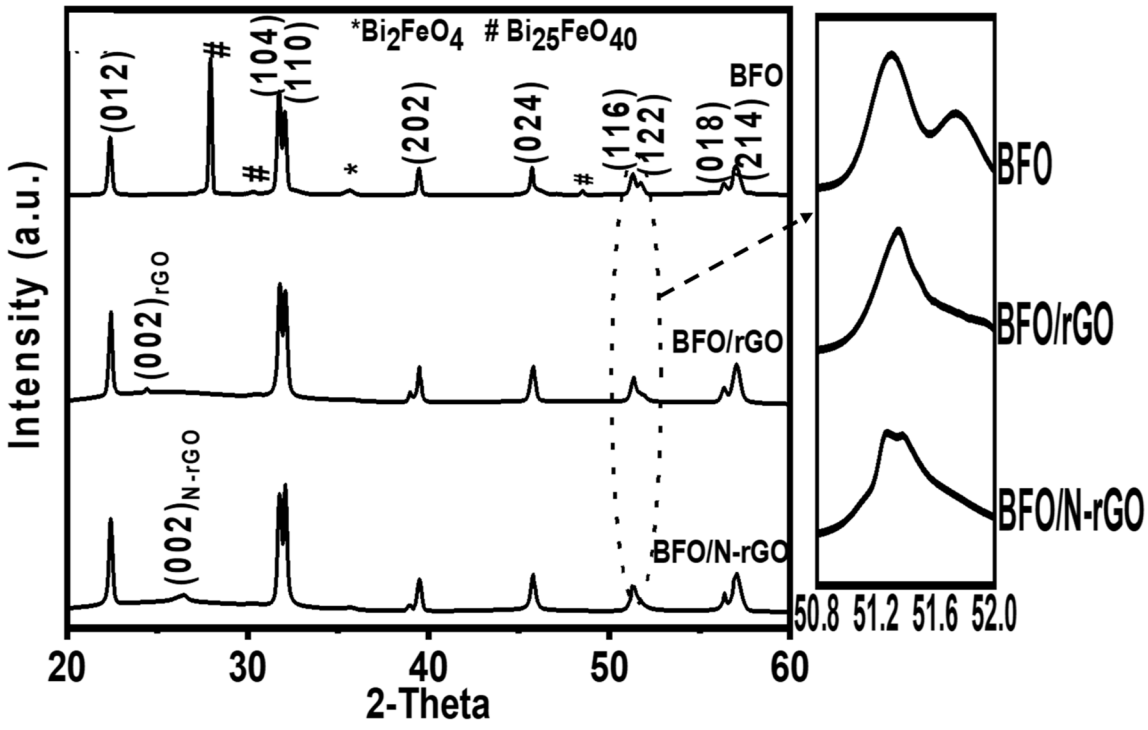

Fig. 4.1. 2 XRD patterns of BFO, BFO/rGO, and BFO/N-rGO; Inset shows the enlarge version around 2-theta equal to 51 degrees.

4.1.2 FTIR Studies

The FT-IR spectra of samples are shown in Fig. 4.1.3 and 4.1.4. The GO spectrum (Fig. 4.1.3) shows a peak at 1038 cm^{-1} corresponding to C-O stretching [210]. Peaks at 1174 and 1390 cm^{-1} are ascribed to C-OH stretching and C-OH bending, respectively [211].

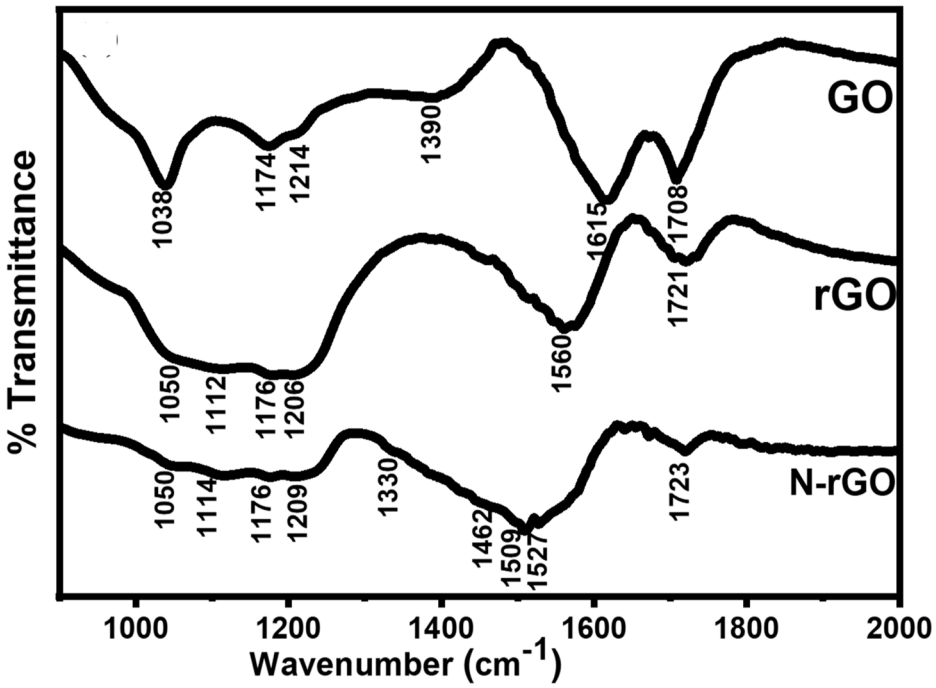

Fig. 4.1. 3 FTIR Spectra of GO, rGO, and N-rGO.

The carbonyl groups are observed at 1708 and 1614 cm^{-1} as C=O stretching and vibration of C=C, respectively, in GO [212]. The intensity of peaks at 1038, 1174, and 1390 cm^{-1} have decreased, which ascribe the elimination of attached oxygen-containing functional groups from graphene oxide and also confirms the reduction of GO. The peak at 1605 cm^{-1} in rGO shows a stretching vibration of C=C [213]. Spectra of N-rGO shows the absorption band at 1527, 1510, and 1462 cm^{-1} are assigned to C=C functional groups (the stretching vibration of C) of sp^2 hybridized carbon atoms of graphene, N-H deformation and asymmetric vibration of C-N, respectively [214]. A peak at 1176 cm^{-1} is ascribed to C-N bond (asymmetric stretching vibration), which overlaps with C-OH

bending [214]. In the spectra of N-rGO, a broad valley appears from 1400 cm^{-1} to 1600 cm^{-1}, which is due to the stretching vibration of C=C and and N-H Bending [215]. Spectra of the prepared sample are shown in Fig. 4.1.4. The absorption in BFO at ~530 cm^{-1} and ~839 cm^{-1} have been attributed to the Bi-O and Bi-Fe bond vibrations. Similar observations have been described by Paschuta et al. [216] for Bi-O in BiO_6 unit and Bi-Fe bond vibration. The absorption at ~550 cm^{-1} and ~581 cm^{-1} are attributed to Fe-O stretching of FeO_6 group and Fe-O-Fe bending in the perovskite structure, respectively. The absorption peaks are consistent with Voll et al. (2006) [217]. An absorption peak ~639 cm^{-1} exhibit Fe-O stretching in FeO_4 group, which is due to the secondary phase of bismuth ferrite (Bi_2 Fe_4O_9) [218]. Oserved functional groups of all the samples are given in Table 4.1.1.

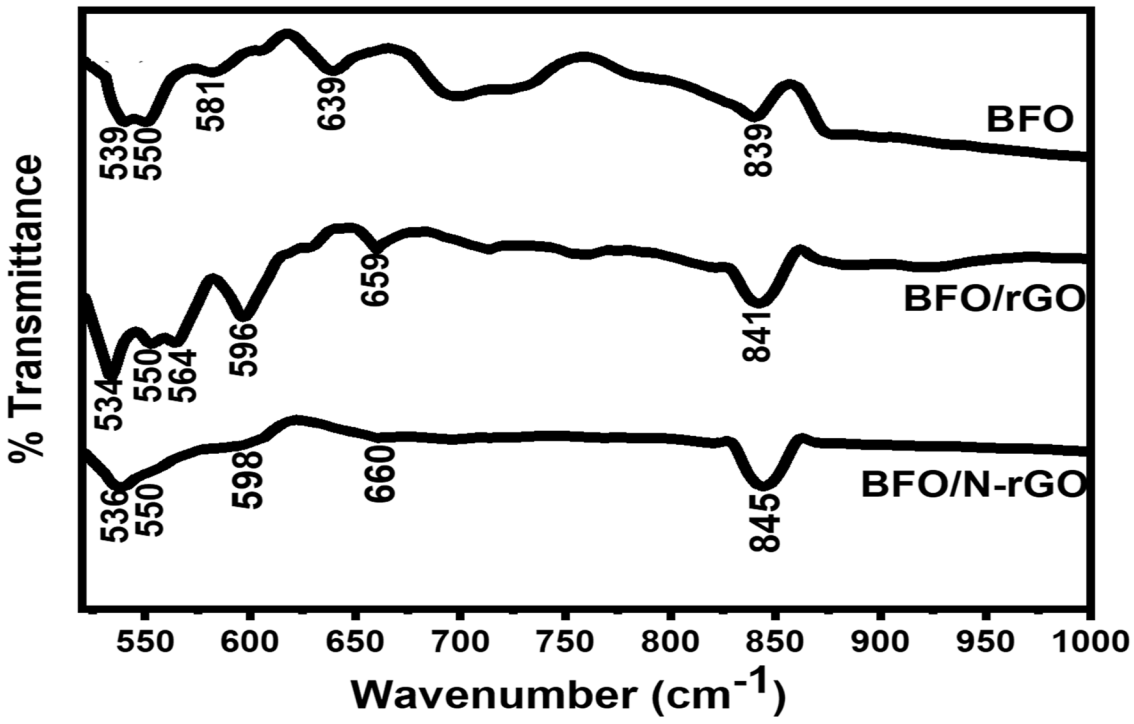

Fig. 4.1. 4 FTIR Spectra of BFO, BFO/rGO, and BFO/N-rGO.

Table 4.1. 1 Observed functional groups by FTIR Spectroscopy

Functional groups	**Absorption peaks (cm^{-1}) in sample**					
	GO	rGO	N-rGO	BFO	BFO/rGO	BFO/N-rGO
Bi-O strech in BiO6	-----	-----	-----	540	533	538
Fe-O strech in FeO6	-----	-----	-----	550	550	552
Fe-O-Fe bending	-----	-----	-----	581	596	596
Fe-O streching FeO4	-----	-----	-----	639	659	660
Bi-Fe	-----	-----	-----	839	841	845
C-O epoxy group	1038	1050	1050	-----	-----	-----
R-O-R asymmetric strech in ether	-----	1112	1114	-----	1119	-----
C-O-H strech in alcohol	1174	1174	-----	-----	-----	-----
C-N asymmetric streaching	-----	-----	1176	-----	-----	1176
R-COOR strech in ester	1214	1206	1209	-----	1234	-----
C-O-H bending in alcohol	1390	-----	1330	-----	1460	-----
C-N asymmetric vibration	-----	-----	1462	-----	-----	1384

C=C graphite	1614	1560	1527	-----	1561	1552
N-H deformation	-----	-----	1509	-----	-----	-----
C=O carbonyl group	1708	1721	1723	-----	1716	-----

4.1.3 UV- DRS analysis

The bandgap of BFO is ascertained by the difference in energies between the valance band edge and conduction band edge. Bi 6p hybridizes with O 2p to form valance band edge and Fe 3d form conduction band edge [219]. Fig. 4.1.5 depicts the UV-DRS spectra of the prepared catalysts. It is observed that bandgap excitation begins at ~ 600 nm in all catalysts. Two striking features were observed. Firstly, BFO/rGO and BFO/N-rGO exhibited higher optical absorption than BFO. The absorption was highest in BFO/N-rGO where N-rGO was used as support. Secondly, the bandgap became narrow after incorporation of rGO (BFO/rGO) and N-rGO (BFO/N-rGO) with BFO. The narrowing was more when N-rGO was used as support. This is due to $\pi - \pi^*$ transition of aromatic carbon and π band associated with p_z orbital of C to π^* band associated with p_z orbital of N [220].

The direct band-gap energies of catalyst were calculated by Tauc's equation (Eq. 1):

$$(\alpha h\vartheta)^2 = B\left(h\vartheta - E_g\right) \quad (4.1.1)$$

Where Eg, ν, α, h and B are bandgap energy, light frequency, absorption coefficient, Plank constant and a constant, respectively. The Band gaps of the catalysts were obtained from plots of $(\alpha h\vartheta)^2$ vs hv, as shown in Fig. 4.1.6. The band gaps were calculated by the extrapolating the linear portion of $(\alpha h\vartheta)^2$ vs hv plots at the point α=0 and the values are given in Table 4.1.2. The decrease in the bandgap of BFO is mainly due to (i) the compositional change (oxygen vacancy, interaction with other elements)

and, (ii) the resistance to charge transfer from coordinating oxygen to Fe ion [221]. In this study, the bandgap of catalysts was observed in a order viz., BFO/N-rGO < BFO/rGO < BFO. Band gap of BFO/rGO and BFO/N-rGO become narrow due a new band appear near the Fermi level which is originated by C 2p state of graphene and C 2p orbitals partially hybridized with both valance band as well as conduction band [222]. This observation shows that there is a chemical interrelation between BFO and support (rGO/N-rGO).

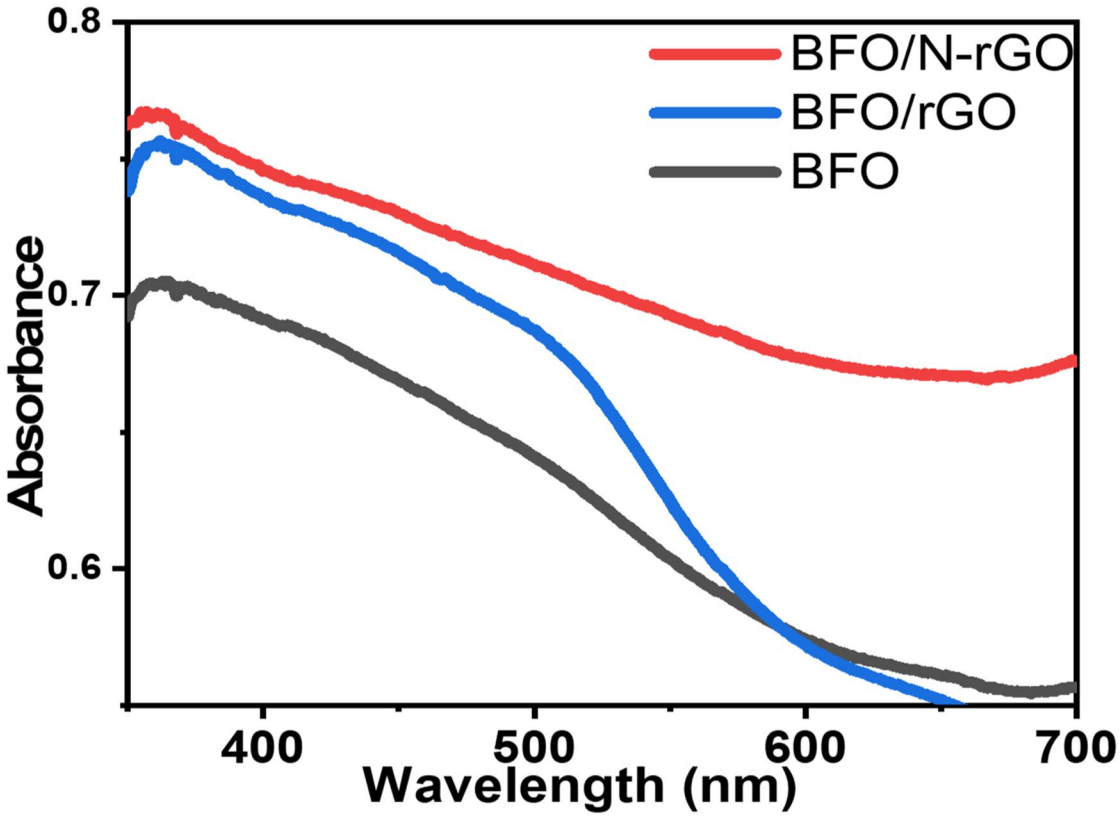

Fig. 4.1.5 DRS of BFO, BFO/rGO, and BFO/N-rGO.

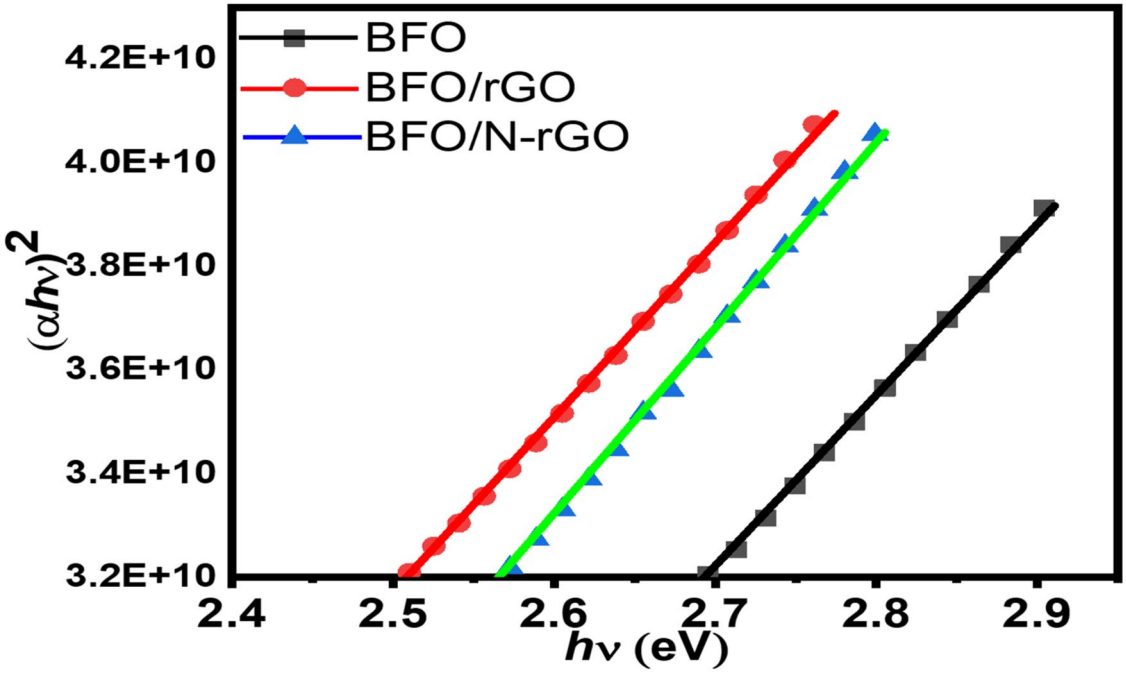

Fig. 4.1. 6 Tauc's Plot of BFO, BFO/rGO, and BFO/N-rGO.

Table 4.1. 2 Band gap, average crystallite size and particle size of BFO, BFO/rGO, and BFO/N-rGO.

Catalyst	Band Gap	Average crystallite size by XRD	Particle size by TEM
BFO	1.72	44	46
BFO/rGO	1.67	48	72
BFO/N-rGO	1.56	49	68

4.1.4 TEM analysis

Detailed morphology was explored by using TEM and HR-TEM. Fig.4.1.4 (a-f) shows that BFO particles are dispersed on the surface of exfoliated rGO and N-rGO. Average particle size was calculated by using ImageJ software. BFO, BFO/rGO and BFO/N-rGO showed 46, 72, and 68 nm, respectively (Table 4.1.2). Comparison of particle size of BFO/rGO and BFO/N-rGO with XRD results revealed that there is a significant agglomeration of BFO particles on the surfaces of supports (rGO/N-rGO). Interplanar spacing (d-value) calculated from HR-TEM images matched with BFO, rGO and N-rGO (Fig. 4.1.7 (d-f)).

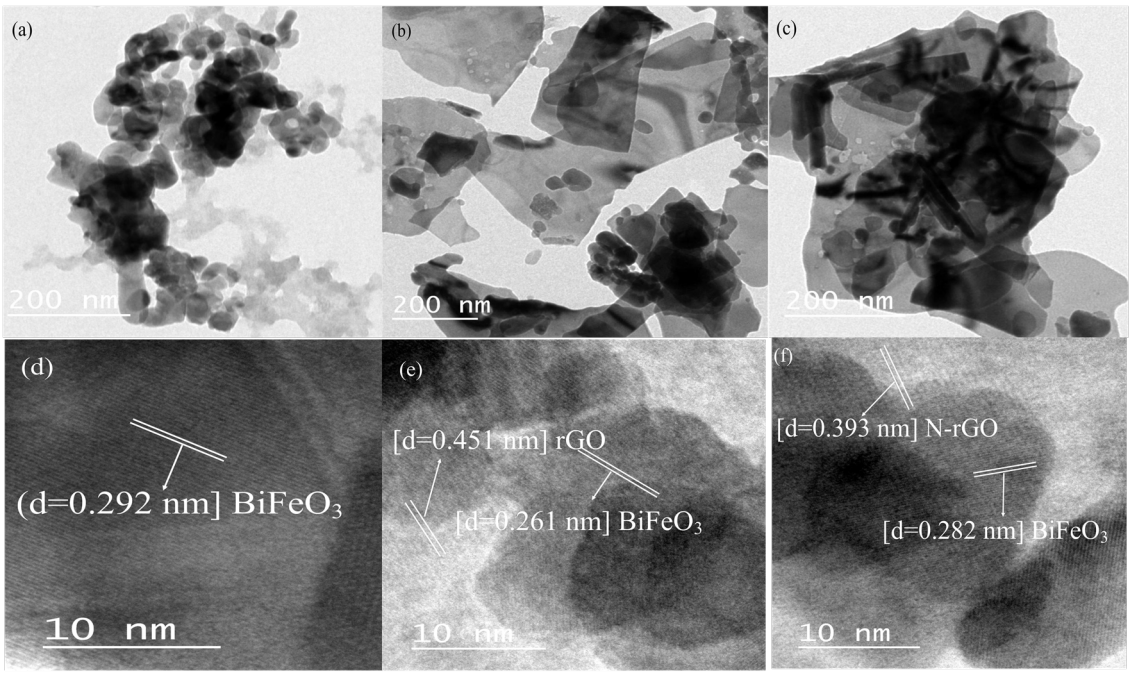

Fig. 4.1. 7 TEM images of (a) BFO, (b) BFO/rGO, and (c) BFO/N-rGO; HR-TEM of (d) BFO, (e) BFO/rGO. and (f) BFO/N-rGO.

4.1.5 XPS Studies

X-ray photoelectron spectroscopy (XPS) was used to analyze the presence of chemical elements and their interactions on the surface of rGO, N-rGO, and catalysts. Lorentzian-Gaussian method was used to deconvolute the peaks. Fig. 4.1.8 (a-d) shows that the XPS signals from the core level C 1s of rGO, N-rGO, BFO/rGO and BFO/N-rGO. C 1s peak was deconvoluted, and peak positions are given in Table 4.1.3. The peak at ~ 284.6 eV, corresponding to C-C (sp^2), is distinct in all samples. Peaks at ~ 285.5 eV, ~ 289.0 and ~ 286.5 eV are assigned to C-H, C-OOH and C-O as well as C-N, respectively. Therefore, peak (~286.5 eV) in N-rGO and BFO/N-rGO may be due to both C-O and C-N [223].

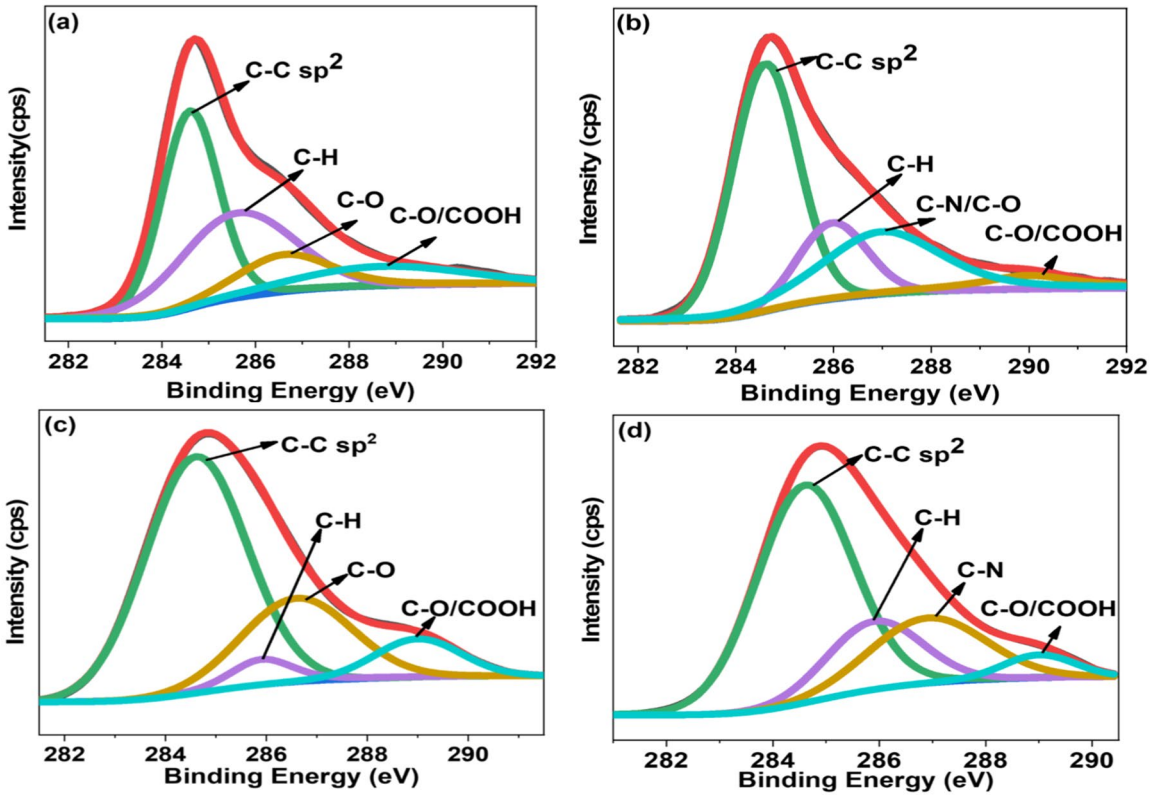

Fig. 4.1. 8 XPS spectra of C 1s (a) rGO, (b) NrGO, (c) BFO/rGO, (d) BFO/N-rGO.

A high-resolution N1s peak appears in N-rGO, which gives the direct evidence of nitrogen doping in graphene Fig. 4.1.9 (a and b). The peak of N1s was deconvoluted into three peaks centred at 398.6 (pyridinic N), 400.1 (pyrrolic N) and 401.6 (graphitic N) which indicate that nitrogen atom is incorporated with graphene successfully [224]. Fig. 4.1.9 shows these three bonds in BFO/N-rGO. Nitrogen provides Lewis-base sites which offer more active sites to adsorb the dye [225]. It could be one of the factors for the improved photocatalytic performance of BFO/N-rGO.

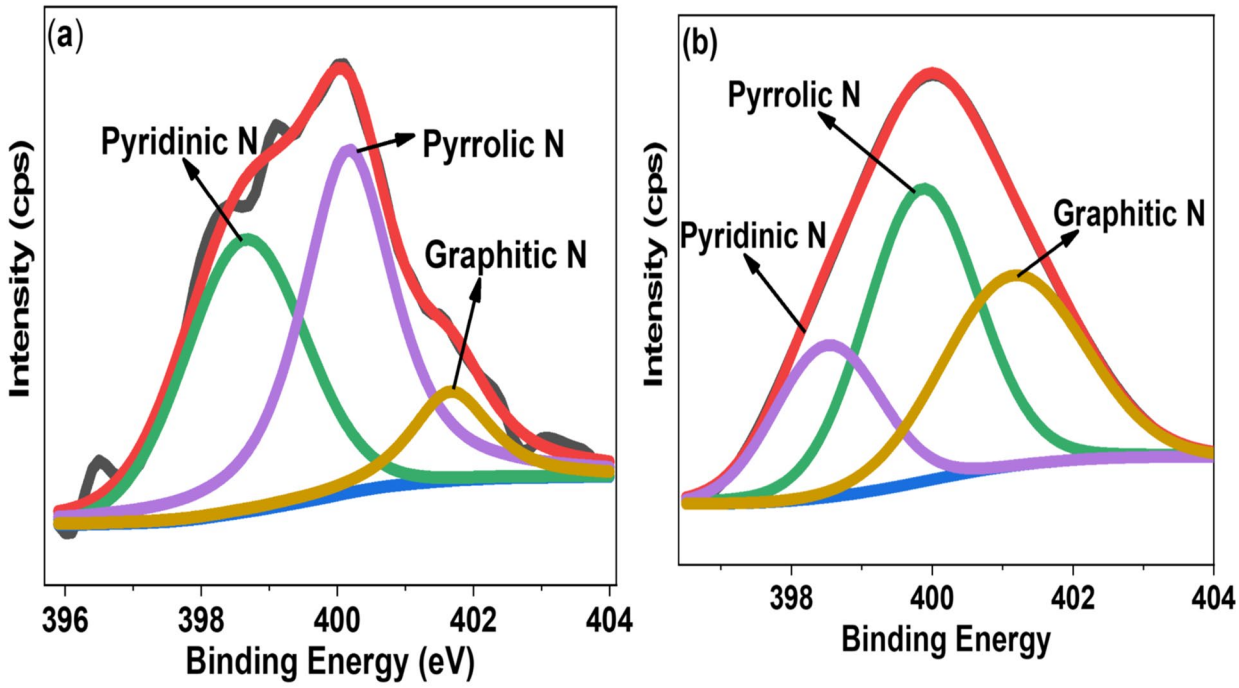

Fig. 4.1. 9 XPS spectrum of N1s (a) NrGO, (b) BFO/N-rGO.

Table 4.1. 3 Binding energy of C 1s and O 1s electrons in rGO, N-rGO, BFO, BFO/rGO and BFO/N-rGO.

Sample	**Binding energies (eV) of C 1s**				**B.E (eV) of O 1s**			
	C-C (sp^2)	C-H	C-O/ C-N	C-O/COOH	Fe-O	Bi-O	C-OOR	C-O
rGO	284.6	285.6	286.6	288.7	-----	-----	530.8	533.2
N-rGO	284.6	285.9	286.9	289.9	-----	-----	530.6	533.0
BFO	-----	-----	-----	-----	529.3	530.1	-----	-----
BFO/rGO	284.6	285.9	286.6	289.0	529.3	530.1	531.4	532.7
BFO/N-rGO	284.6	285.9	286.9	289.0	529.2	529.9	531.5	532.8

Fig. 4.1.10 (a-e) shows the XPS spectra of O 1s for rGO, N-rGO, BFO, BFO/rGO and BFO/N-rGO. Binding energies of O 1s electrons for different bonds in the materials are given in Table 4.4. In case of both rGO and N-rGO, only two peaks are observed, and these are assigned to C-OOR (~530.6 eV) and C-O (~533 eV) [224]. Catalysts (BFO, BFO/rGO and BFO/N-rGO) exhibit peaks representing to iFe-O (~529.3 eV) and Bi-O (~530 eV) [226]. Position of peaks corresponding to C-O and C-OOR were shifted in BFO and BFO/rGO with respect to those of rGO and N-rGO, respectively. This indicates redistribution of electron density due to the electronegativity of oxygen more than the electronegativity of bismuth which attributes chemical interaction between BFO and rGO/N-rGO. Therefore, the binding energy of C-O and C-OOR shifted toward lower

binding energy. Such a chemical interaction will result in the formation of heterojunction between BFO and rGO/N-rGO, and also prevent to charge recombination [227].

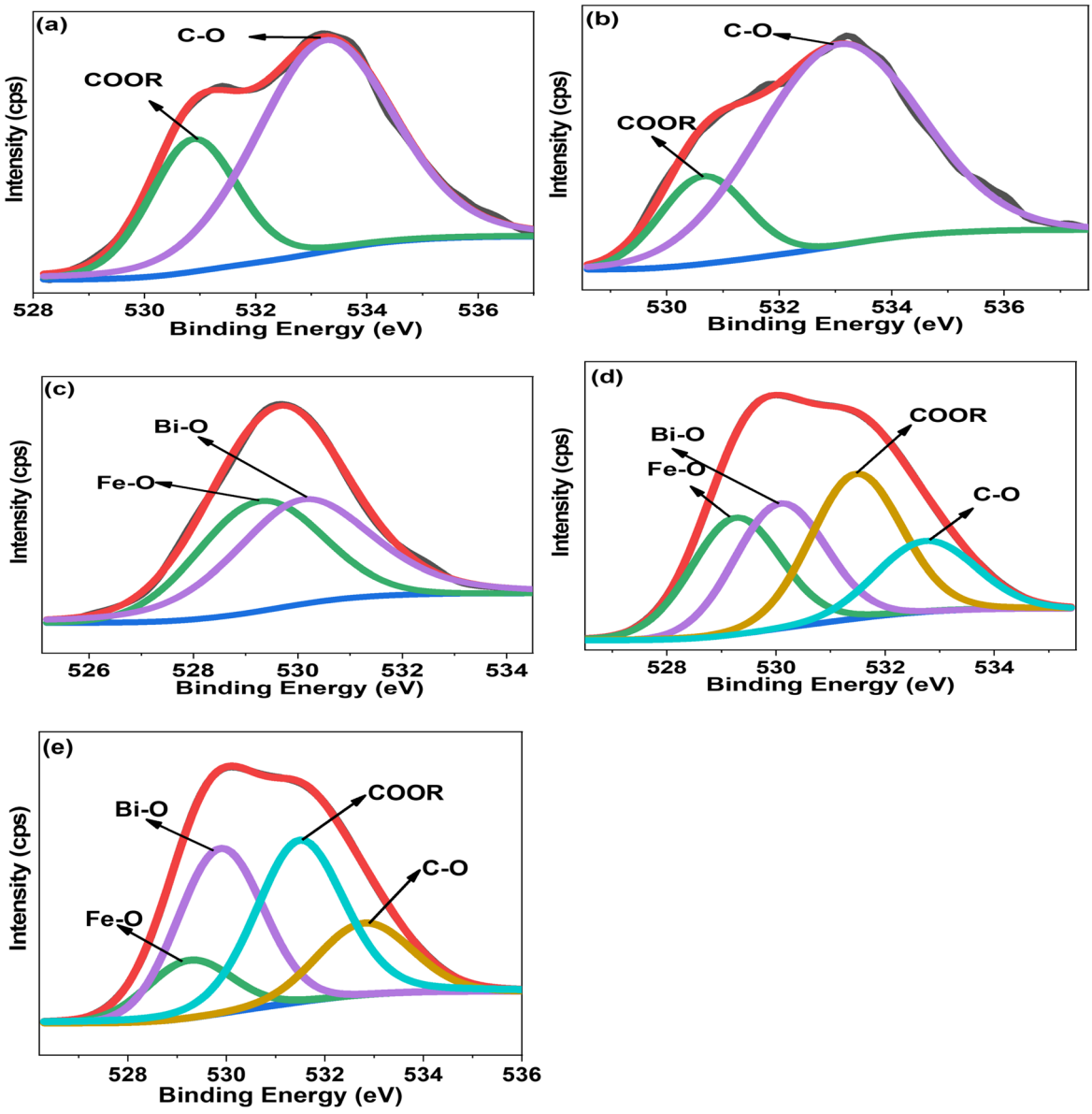

Fig. 4.1. 10 XPS spectra of O 1s (a)rGO (b) NrGO (c) BFO (d) BFO/rGO (e) BFO/N-rGO.

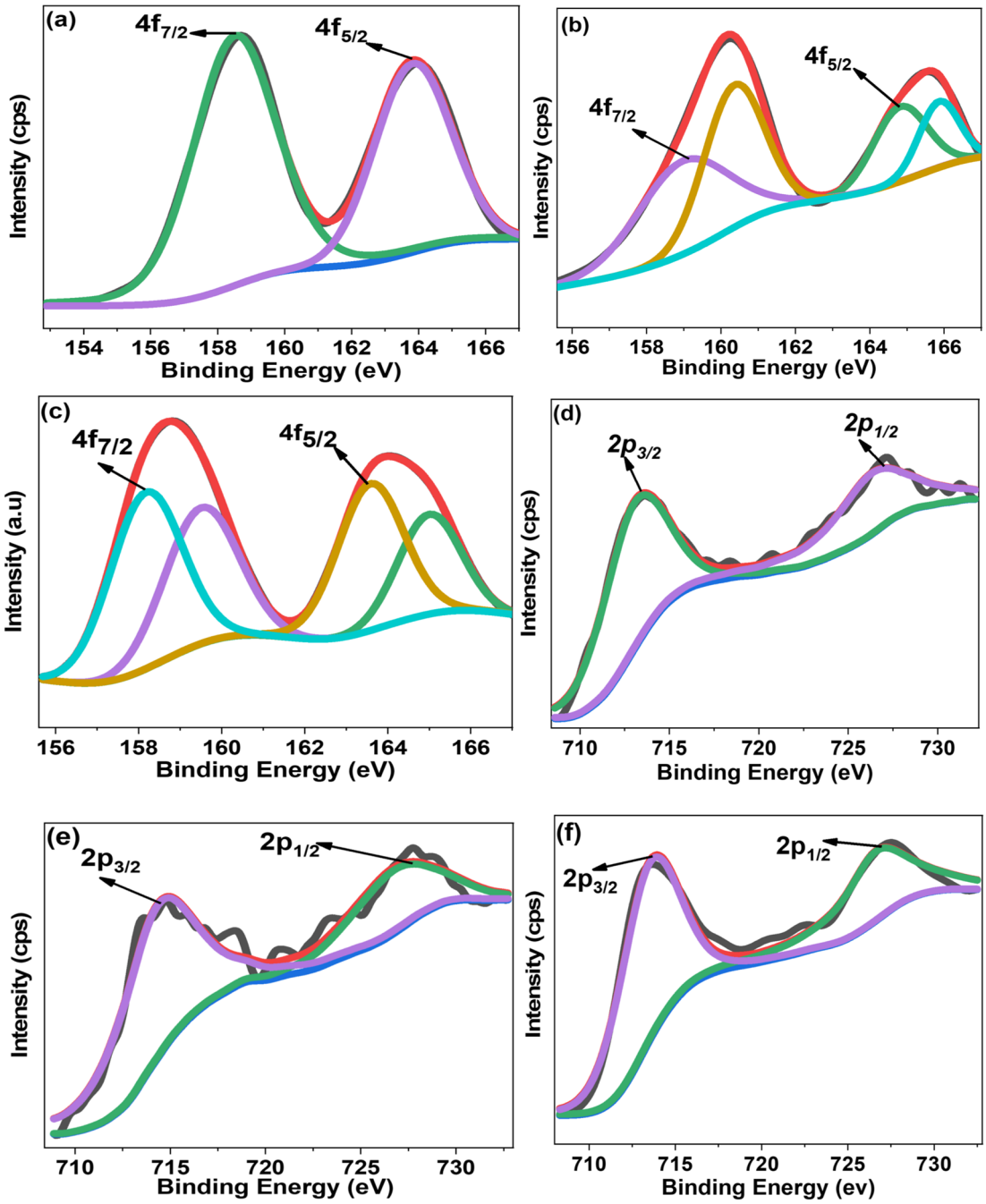

Fig. 4.1. 11 XPS spectra of Bi 4f in (a) BFO (b) BFO/rGO (c) BFO/N-rGO; Fe 2p in (d) BFO (e) BFO/rGO (e) BFO/N-rGO.

Fig. 4.1.11 (a-c) describes the XPS spectra of Bi 4f of the catalysts. Peaks of Bi 4f in BFO appear at 158.2 eV and 163.5 eV which point out a spin-orbit splitting of about 5.3 eV. The peaks designate that bismuth is in Bi^{+3} state [228]. Two additional peaks at ~160.3 and ~165.8 eV appear in BFO/rGO and BFO/N-rGO which are rGO and N-rGO supported, respectively. The binding energy of bismuth increases owing to a decrease in electron density because the electronegativity of bismuth is less than the electronegativity of carbon and oxygen [229]. It can be attributed to the formation of Bi-O-C bond due to the interaction of graphene/ nitrogen-doped graphene. The peak ratios of $4f_{7/2}$ were computed for BFO/rGO and BFO/N-rGO. The higher value of ratio indicates higher chemical interaction of bismuth with N-rGO as compared with rGO [204]. Fig. 4.1.11 (d-f) explains Fe 2p peaks at 710.8 eV and 723.8 eV, which represented spin-orbital interactions of Fe $2p_{3/2}$ and Fe $2p_{1/2,}$, respectively. Difference between these two spin orbitals is 8.0 eV, which confirms that Fe^{+3} is present in all photocatalysts [226]. However, no peak is observed at 709.5 eV, which indicates the absence of Fe^{+2} in the samples [230]. Binding energies of Bi^{+3} and Fe^{+3} are tabulated in Table 4.1.4.

Table 4.1. 4 Binding energy of Bi^{+3} and Fe^{+3} electrons in BFO, BFO/rGO, and BFO/N-rGO.

Sample	**B.E (eV) of Bi^{+3}**				**Ratio**	**B.E (eV) of Fe^{+3}**	
	First-Doublet(I)		Second-Doublet(II)		$[4f_{7/2}]_{II}/[4f_{7/2}]_{I}$		
	$4f_{7/2}$	$4f_{5/2}$	$4f_{7/2}$	$4f_{5/2}$		$2p_{3/2}$	$2p_{1/2}$
BFO	158.5	163.8	-----	-----	-----	713.0	726.3
BFO/rGO	158.9	164.8	160.3	165.8	0.97	714.3	726.7
BFO/N-rGO	158.9	163.6	160.1	165.1	1.02	713.5	726.6

4.1.6 Photoluminescence studies

Fluorescence spectra of photocatalysts were examined to study the recombination rate of the photogenerated electron-hole pairs. Photoluminescence (PL) emission mainly upraises from the recombination of photoinduced electron-hole pairs in photocatalysts [151]. Fig. 4.1.12 illustrates the PL of catalysts assessed with an excitation wavelength of 200 nm and the emission peak of BFO at 529 nm. The fluorescence spectra of all photocatalysts follow a similar curve with different intensity, which attributes a prominent role of BFO in photoluminescence generation. Compared with BFO and BFO/rGO, BFO/N-rGO shows much weaker PL intensity attributed to a slow rate of recombination of electron-hole pairs. This result connotes that upon generation of the photo-induced electrons in bismuth ferrite are quickly transported into rGO/N-rGO, leading to suppress charge recombination and thus improved photocatalytic performance. It proved that BFO/N-rGO had the most prominent photocatalytic activity followed by BFO/rGO. BFO showed the lowest activity.

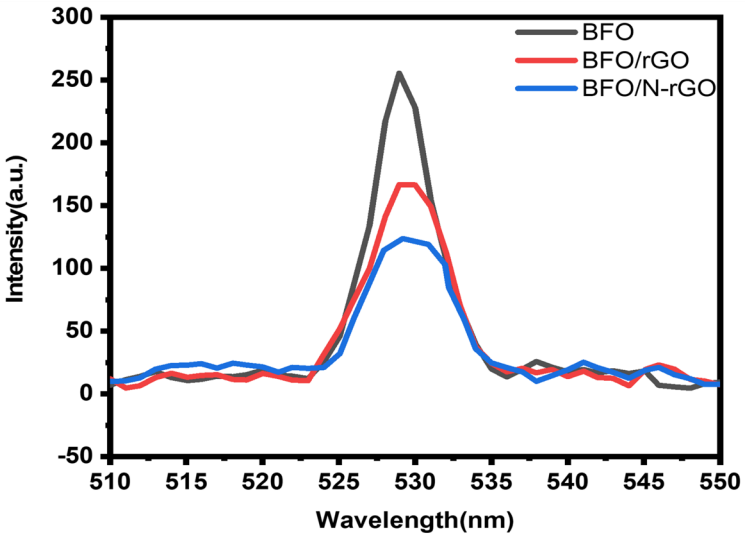

Fig. 4.1. 12 PL Spectra of BFO, BFO/rGO, and BFO/N-rGO.

4.1.7 Electrochemical impedance spectroscopy (EIS) Studies

Electrochemical impedance spectroscopy (EIS) was performed to determine the interfacial charge transfer resistance of catalysts [229]. Fig. 4.1.13 shows the Nyquist plots of the catalysts. Smaller arc radius indicates low charge transfer resistance. Hence low recombination and an efficient charge transfer occur through the liquid-solid interface for the photocatalytic degradation [231]. The arc radius of the Nyquist plot follows the trend in increasing order as BFO/N-rGO < BFO/rGO < BFO. This study shows that BFO/N-rGO has the lowest interfacial charge transfer resistance and effectively restrain the recombination of electron-hole pairs, leading to enhanced photocatalytic performance.

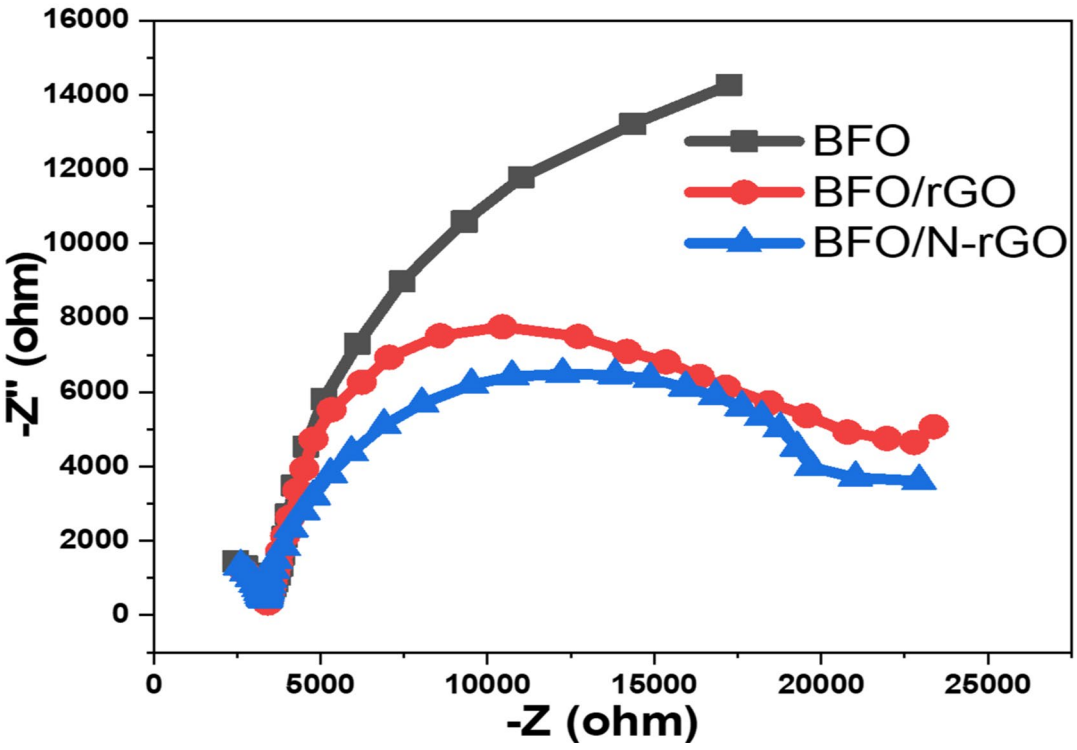

Fig. 4.1. 13 Nyquist plots of BFO, BFO/rGO, and BFO/N-rGO.

4.1.8 Mott-schottky Analysis

Mott-Schottky (M-S) analysis was carried out to understand the effect on Fermi level of BFO after incorporation with graphene. M-S plots of the catalysts are shown in Fig. 4.1.14. Junction capacitance was measured by applying the potential from 0.0 to 1.0 V versus SHE at a constant frequency (1.0 kHz) for all catalysts. The flat band potentials and charge densities, for all the samples, were computed by using Eq. 2 [232].

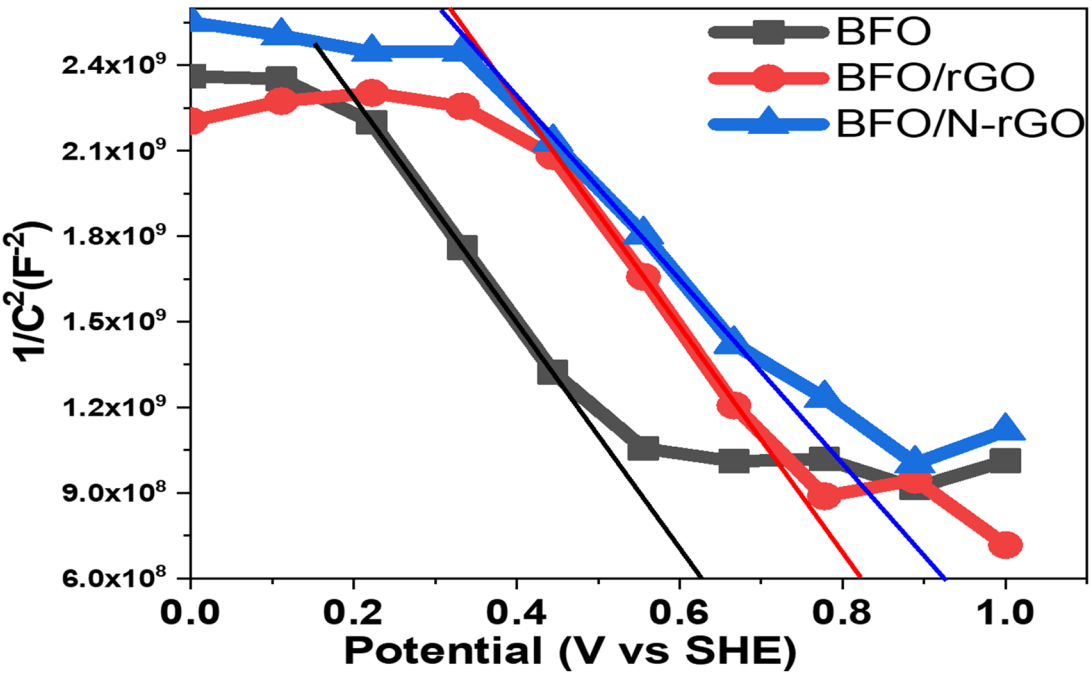

Fig. 4.1. 14 Mott-Schottky plots of BFO, BFO/rGO, and BFO/N-rGO.

$$\frac{1}{C^2} = \frac{2}{\epsilon_0 \epsilon_r \, eN_D A^2}\left(V - V_{fb} - \frac{KT}{q}\right) \qquad (4.1.2)$$

Where, C is the junction capacitance, K is the Boltzmann's constant (1.38×10^{-23} J/K), N_D is the charge carrier density, A is the surface area of the electrode (25×10^{-6} m^2), T is the absolute temperature, e is the electron charge (1.603×10^{-19}C), ε_0 is the permittivity of the vacuum (8.854×10^{-12} Fm^{-1}), ε is the dielectric constant of BFO (~65)

[105], V_{fb} is the flat band potential, and V is the applied potential. The charge carrier density (N_D) and flat band potential were computed from the M-S curve by evaluating the slope of a linear portion of the curve and the interception of a linear portion with the potential axis. At room temperature and one-atmospheric pressure, the numerical value of KT/q is negligible and also can be calculated. Linear portion and the nature of the slope of the M-S plots attributed to p-type semiconductor [204]. Flat band potential of BFO is 0.62 V, and after incorporation of rGO and N-rGO with BFO flat-band potentials increased (Table 4.1.5). It shows that BFO/N-rGO has the highest flat band potential (0.90 V) and thus highest charge density (9.05 x 10^{27} cm^{-3}) which assures a sufficient band bending and effective charge segregation. This charge separation leads to an enhanced photocatalytic performance owing to enough number of photoinduced electron-hole pairs being accessible for the photocatalytic degradation.

Table 4.1. 5 Flat band positions and carrier concentrations for BFO, BFO/rGO and BFO/N-rGO.

Catalyst	**Flat band potential (V_{fb},V) vs SHE**	**Charge carrier density(N_D,cm^{-3})**
BFO	0.62	8.79 x 10^{27}
BFO/rGO	0.81	8.82 x 10^{27}
BFO/N-rGO	0.90	9.05 x 10^{27}

4.1.9 Photocatalytic performance

4.1.9.1 Effect of catalyst concentration

Economical point of view, catalyst loading optimization is a very important parameter and it also assure maximum utilization of light. The catalyst loading effect was investigated by varying BFO concentration from 40 to 200 mg. L^{-1} in photocatalytic degradation process. 10 ppm RhB solution (250 mL) was taken in all the reactions and UV light was used as a light source. From Fig 4.1.15, it is clearly seen that on increasing catalyst loading photocatalytic degradation efficiency is increases from 40 to 120 mg. L^{-1} catalyst loading due to mainly two reason viz., high absorption of light on catalyst surfaces and increasing no. of adsorption sites [233, 234]. This resulted into enhanced generation of reactive species and increased RhB adsorption on catalyst surface leading

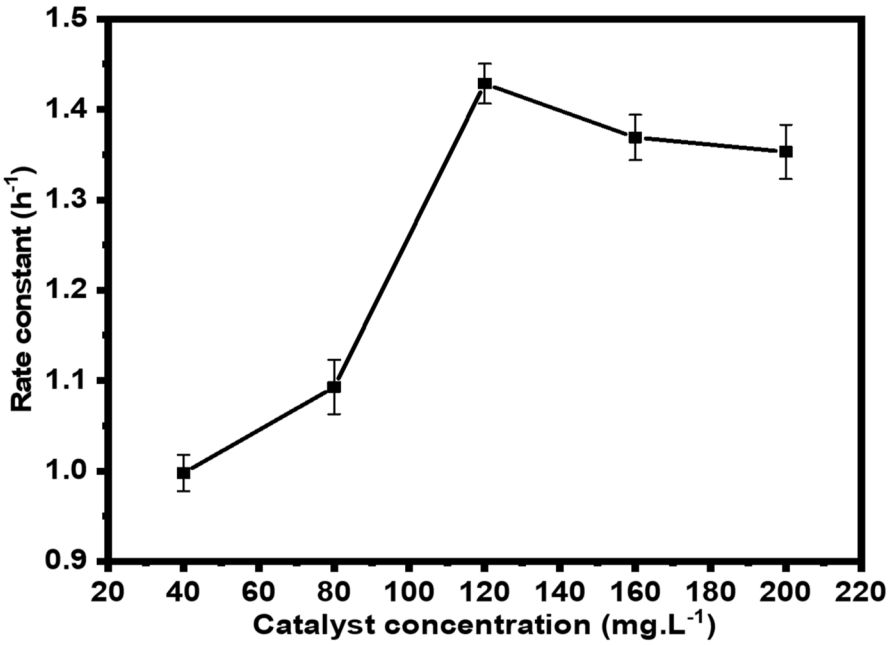

Fig. 4.1. 15 Effect of catalyst loading.

to increased degradation efficiency. However, beyond 120 mg. L^{-1} catalyst loading, degradation efficiency decreases due to mainly agglomeration of catalyst particles and increase turbidity in the solution. Agglomeration of catalyst particles lead to

unavailability of a part of adsorption site for dye and increased turbidity in the solution enhances light scattering leading to decreased light penetration during the reaction [235, 236]. In this study, 120 mg. L^{-1} catalyst loading was found as an optimum catalyst concentration. Hence, all further studies were done by using the optimum loading of 120 mg. L^{-1}.

4.1.9.2 Effect of dye concentration

To study the effect of initial dye concentration, photocatalytic degradation of RhB was carried out by varying initial RhB solution concentration from 2.5 to 20 ppm in presence of BFO (120 mg.L^{-1}) under UV light. From Fig. 4.1.16, RhB degradation rate increases with increase initial concentration from 2.5 ppm to 10 ppm and from 10 to 20 ppm concentration range degradation rate decreases. In photocatalytic degradation process,

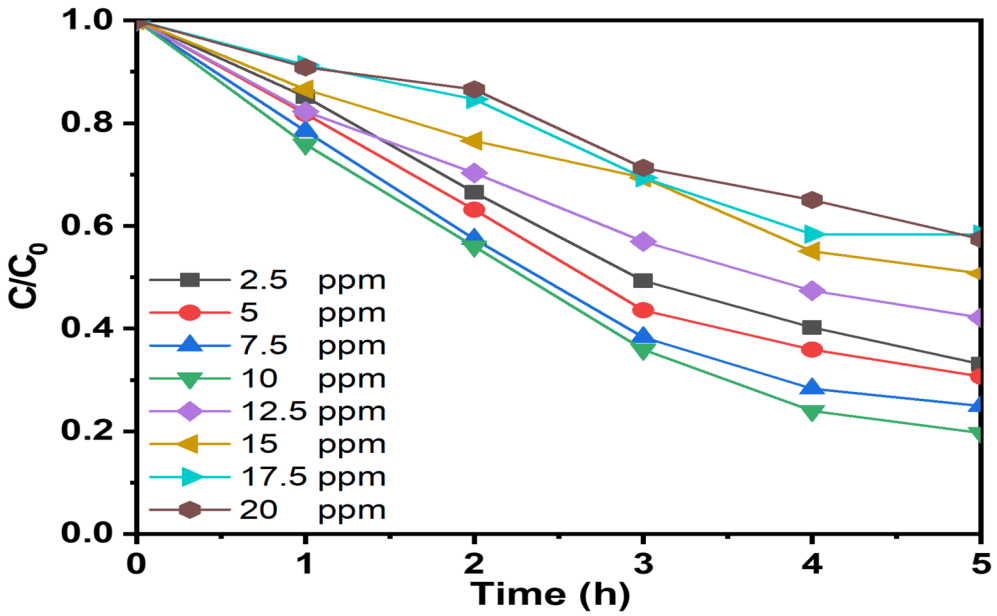

Fig. 4.1. 16 Effect dye concentration (Catalyst loading 120 mg.L^{-1}, pH= 4.3).

two processes occur parallelly viz., migration of photogenerated electron hole pairs and reaction of dye with reactive species. Mass transfer between solid/liquid interface and

active adsorption site on the catalyst surface play very important role in dye degradation process [237, 238]. Therefore, at low initial RhB solution concentration (from 2.5 to 10 ppm) active adsorption sites are not limiting factor for degradation reaction. Hence, in this range degradation rate is directly proportional to RhB solution concentration. In contrast to that, in the range 12.5 to 20 ppm RhB solution, all the active adsorption sites of the catalyst are occupied, then dye concentration is not the important parameter for the degradation process. Therefore, beyond optimum initial RhB solution concentration photocatalytic degradation efficiency decreases. In this study, 10 ppm RhB solution concentration was found optimum initial concentration.

4.1.9.3 Effect of pH

In photocatalytic degradation process, pH of the solution is known to affect strongly surface charge of the photocatalyst [239]. Therefore, effect of pH was investigated on photocatalytic degradation of RhB and pH of the solution was varied from 1 to 10 in presence of BFO photocatalyst. As shown in Fig. 4.1.17, it is observed that with decreasing pH as well as increasing pH value from 4.3, the photodegradation rate of RhB greatly increased. Photocatalytic activity depends on adsorption of dye, and adsorption of dyes are highly pH dependent. When pH value of the RhB solution with photocatalyst system is changed, two changes occur in the system viz., charge state of RhB and surface charge of photocatalyst. The pKa of carboxyl group, present in RhB molecule, is 4. Therefore, below the pH value 4, carboxyl group present on RhB become acidic[240]. Beyond pH 4, RhB converted into its zwitterion form (separated positive as well as negative groups) form due to ionization of carboxyl groups[240]. Surface charge on BFO become positive in acidic medium and negative in basic medium leading to enhanced RhB adsorption on the catalyst surface. However, adsorption of RhB in basic medium is less as compared to basic medium due to repulsion between solid surface and COO^-

present in RhB. Hence, photocatalytic activity decreases as compared to acidic medium (pH= 1 to 3).

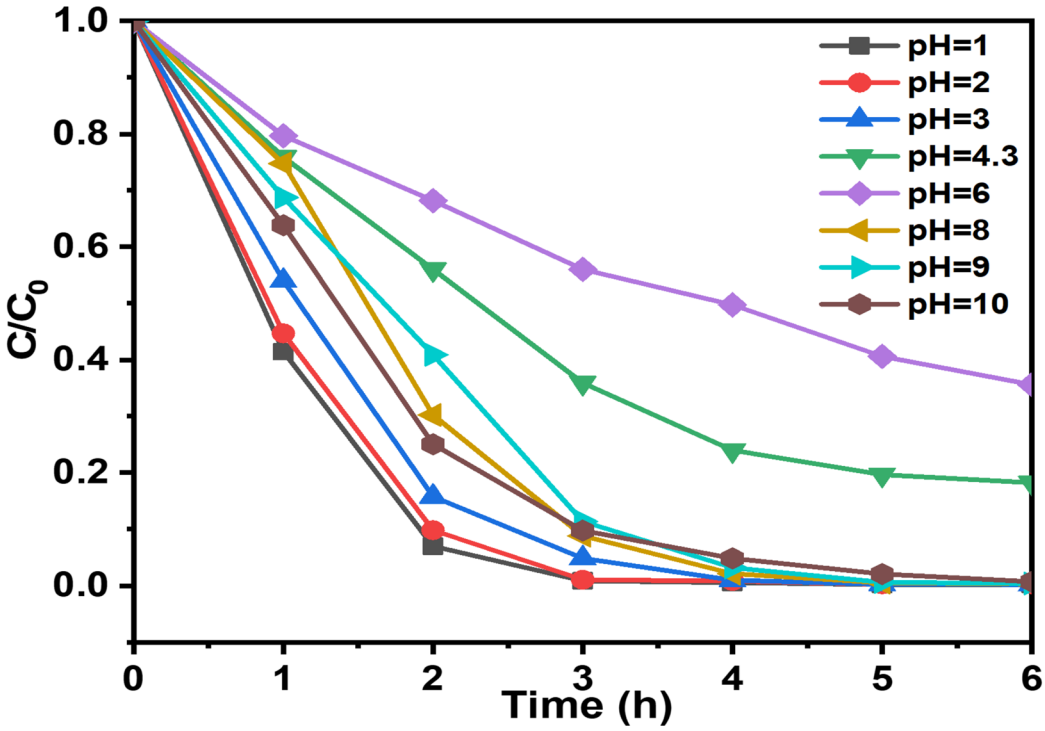

Fig. 4.1. 17 Effect of pH on photocatalytic degradation of RhB.

4.1.9.4 Photocatalytic degradation kinetics

The activity of the catalysts in terms of C_A/C_{A0} Vs time (where C_{A0} and C_A are concentrations of RhB at time t=0 and at any time t, respectively) for RhB degradation is presented in Fig. 4.1.18 a. The initial concentration of RhB was 10 $mg.L^{-1}$, and the amount of catalyst was 120 $mg.L^{-1}$. Earlier similar experiments were carried out without any catalyst and also with rGO and N-rGO only. The drop in the concentration of RhB was negligible even with catalysts under dark conditions in all the three cases. It confirms that the reaction was photocatalytic in behaviour. BFO showed approximately 95% oxidation of RhB within 5 h (Fig. 4.1.18 a). Incorporation of rGO and N-rGO, i.e.,

BFO/rGO and BFO/N-rGO result into improved activity. BFO/N-rGO delivered the best performance, which degraded upto 98.7% in 3h. Corresponding plots of $-\ln C_A/C_{A0}$ vs t is shown in Fig. 4.1.18 b. Plots are linear, which indicates that the first-order equation adequately fits the data. The high activity of BFO/N-rGO is attributed to (a) high charge density (b) efficient photoinduced charge separation due to low electrical resistance and higher band potential and (c) high absorptivity and a lower bandgap. Linear plots were obtained which confirm the first-order kinetics. The slope of the line yielded a value of the chemical rate constant, k. The k value for each catalyst is reported in Table 4. Prior experiments were performed to study the effect of catalyst loading. It should also be mentioned that a high degree of agitation was also maintained and therefore, mass transfer resistance was assumed to be negligible.

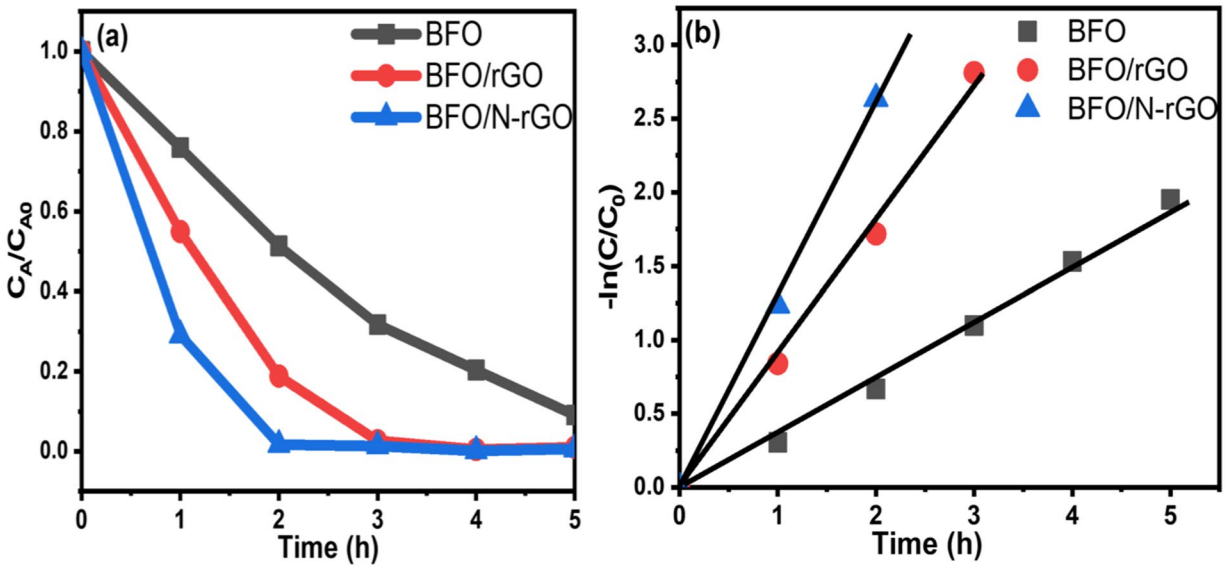

Fig. 4.1. 18 (a)Photocatalytic activity of different materials for the degradation of RhB dye; (b) Reaction kinetics.

Concentration vs time data were used to get the kinetic rate equation. A high degree of turbulence ensured that the kinetics was not affected by diffusional effects. Further, a high flow rate (3 mL/sec) of air was ensured to validate the assumption that liquid was saturated with oxygen. A high degree of agitator ensured the absence of any different resistance, in such conditions rate obtained was exact rate constant. BFO/N-rGO exhibited the highest k among all catalysts (Table 4). The rate constant k for BFO/N-rGO is 15.91 $g^{-1}h^{-1}$, which is five times that for the BFO (3.15 $g^{-1}h^{-1}$).

Table 4.1. 6 Rate constant (k, $g^{-1}h^{-1}$) for BFO, BFO/rGO and BFO/N-rGO.

Catalyst	**Rate constant (k, $g^{-1}h^{-1}$)**
BFO	3.15
BFO/rGO	7.57
BFO/N-rGO	15.91

4.1.9.5 Reactive species in photocatalytic degradation of RhB

Identification of the most active species in the photocatalytic degradation process, scavengers were used with BFO as the photocatalyst. Degradation of RhB can be explained by heterogeneous photocatalysis. It involves the generation of $O_2^{-}$and $OH^{\bullet}$ radicals after reacting with the photoinduced electron (e^-) and hole (h^+), respectively. These reactive species are highly efficient to degrade RhB. 1-4 benzoquinone (1-4 BQ), tert-butyl alcohol (TBA), potassium dichromate (PD) and ammonium oxalate (AO) are used as a scavenger of O_2^{-}, $OH^{\bullet}$, e^- and h^+ respectively [241, 242]. The results in Fig. 4.1.14a shows that all the reactive species e^-, hole (h^+), hydroxyl radical ($OH^{\bullet}$) and superoxide radical ($O_2^{\bullet-}$) are reactive species playing a significant role in the photo-

degradation of RhB. However, after addition of 1-4BQ (1 mmol), the degradation of RhB was reduced up to 56%, showing that superoxide ion plays a relatively important role among other species in the photocatalytic degradation process. Apart from the addition of TBA, PD and AO also caused suppression in the photo-degradation of RhB. The degradation percentage of RhB was up to 49, 46, and 25% respectively after 6 h. Therefore, among these species, $O_2^{\bullet-}$ are the most reactive radicals responsible for the photocatalytic degradation reaction whilst all the species are participating in the degradation of RhB.

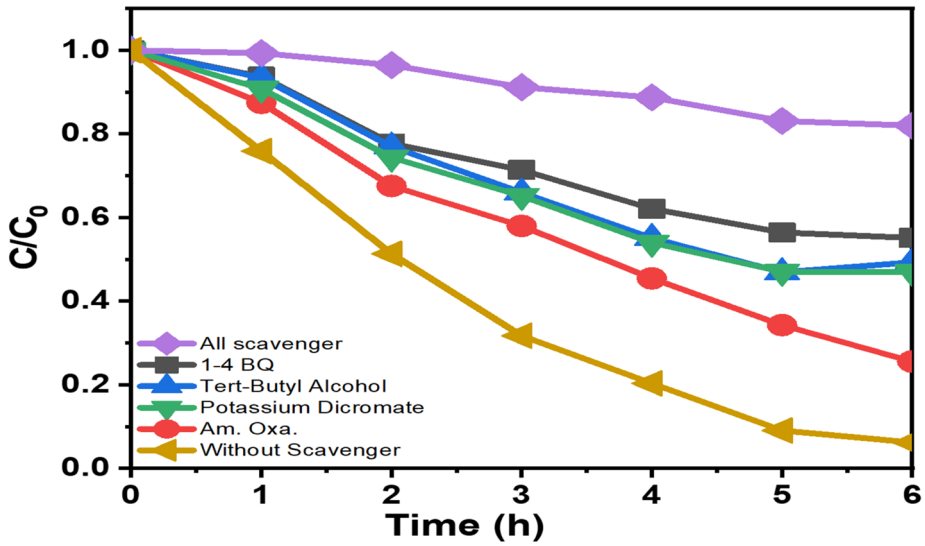

Fig. 4.1. 19 Reactive traping experiment for photocatalytic degradation of RhB.

4.1.9.6 Plausible mechanism of the degradation of RhB

A plausible reaction mechanism for the photocatalytic degradation of RhB has been proposed. Upon illumination of light on the photocatalyst, the valance band (VB) electrons are excited to the conduction band (CB) of BFO and the photoinduced electrons migrated from the bulk to the surface. Electrons are transferred to rGO/N-rGO and finally

to the gas-solid-liquid interface as given below by Eq. 3-5 and. The conduction band electron reactions can be described by Eq. (3-5).

$$BFO + hv \rightarrow BFO(e^- + h^+) \quad (4.1.3)$$

$$rGO/NrGO + e^- \rightarrow rGO/NrGO(e^-) \quad (4.1.4)$$

$$rGO/NrGO(e^-) + O_2 \rightarrow O_2^{-\cdot} + rGO/NrGO \quad (4.1.5)$$

The photogenerated holes on valance band of BFO are responsible for the generation of $OH^{\cdot}$ radical from OH^- at the valance band (Eq. 6).

$$BFO(h^+) + OH^- \rightarrow BFO + OH^{\cdot} \quad (4.1.6)$$

The oxidation potential of reactive oxygen species $O_2^{-\bullet}$ and $OH^{\bullet}$ are -0.33 V Vs NHE and +2.7 V Vs NHE, respectively [312]. Because of the high surface area and high transportation ability of rGO/N-rGO, produced radicals $O_2^{-\bullet}$ and $OH^{\bullet}$ moved from the photocatalyst to the solution interface and degraded RhB into products as described in Eq. (7-9):

$$OH^{\cdot} + RhB \rightarrow Products \quad (4.1.7)$$

$$O_2^{-\cdot} + RhB \rightarrow Products \quad (4.1.8)$$

$$BFO(h^+) + RhB \rightarrow Products \quad (4.1.9)$$

4.1.9.7 Stability of the photocatalyst

Reusability and stability of catalyst are significant parameters for further application. Evaluation of the reusability property of BFO/N-rGO, five cycles of consecutive degradation of RhB were performed by reusing the photocatalyst under the same conditions as mention in section 4.1.10.4.

Fig. 4.1.14b shows the results of photocatalytic degradation of RhB with a minimal loss of activity after five successive experiments. Minimal loss of activity may be owing to the deprivation of active sites on the surface of the catalyst.

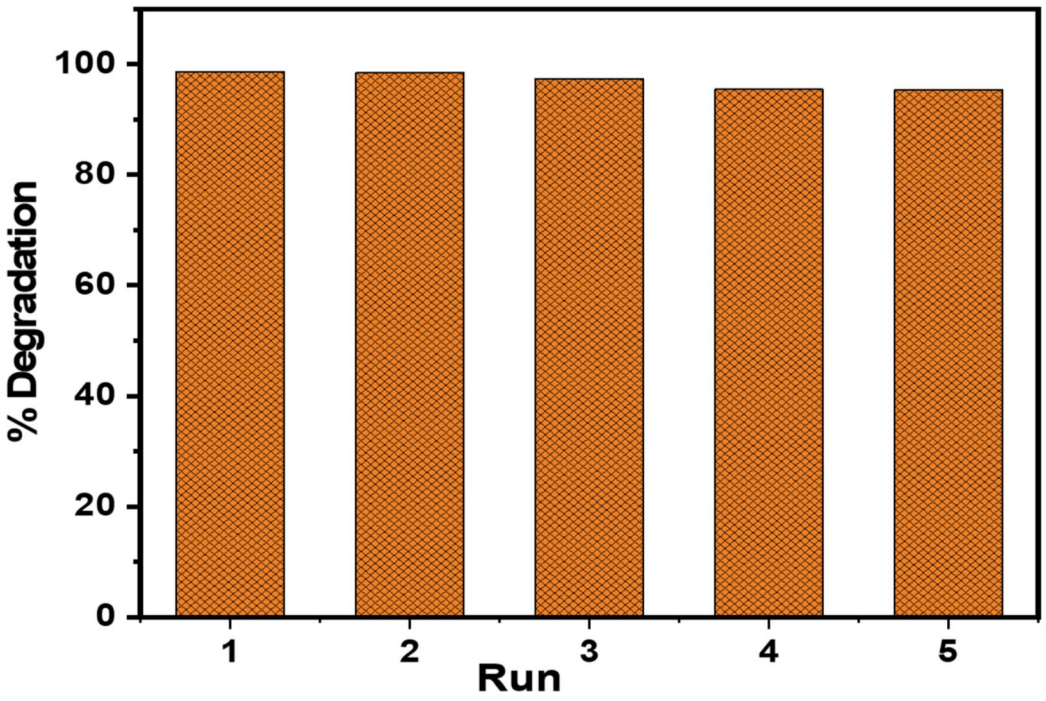

Fig. 4.1. 20 Reusability test.

4.1.10 Summary

XPS analysis revealed the interaction of nitrogen-doped graphene and bismuth ferrite, which facilitate the photoinduced electron-hole pair separation at the surface of BFO. EIS and PL analysis indicated a rapid transformation of electrons from BFO to N-doped reduced graphene due to high electron mobility of N-rGO, which suppresses the recombination of the electron-hole pair. Trapping experiments revealed that $O_2^{\bullet-}$ were found to be the most active radicals responsible for RhB degradation compared to others. Reusability experiments revealed that BFO/N-rGO was found to be a reasonably stable photocatalyst with no distinct loss after five consecutive experimental cycles and has potential future applications.

4.2 Synergistic effect of N-rGO supported Gd-doped bismuth ferrite on photocatalytic degradation of Rhodamine B

Despite the great potential, owing to the recombination of photoinduced electron-hole pairs and low quantum yield, the application of BFO is limited in the contaminated wastewater industry. Extensive research has been carried through to improve the photocatalytic performance of BFO [243]. Doping with metals as well as casting nanocomposites and heterojunctions, leads to improved photocatalytic performance compared to bare BFO. A-site doping in BFO with +3 valence rare earth metal has drawn great attention of researchers because of enhanced electrical property due to the lone pair of Bi $6s^2$ [244].

Rare-earth doped bismuth ferrite resulted in remarkable improvement in photocatalytic properties. Among them, Gd substitution at Bi site in BFO has revealed a phase transformation as well as improving the multiferroic property [245]. N-rGO, as a support, inhibited photoinduced electron hole pair recombination and facilitate lowest resistance toward electron mobility as as discussed in the section 4.1. Therefore, in this section N-rGO supported Gd doped bismuth ferrite (BGFO/N-rGO) heterojunction has been devolved for the photocatalytic degration of RhB. A detailed preparation technique has been discussed in the section 3.3.

4.2.1 XRD studies

Diffraction pattern of BFO revealed (012), (104), (110), (202), (024), (122), (018) and (214) planes (Fig. 4.2.1) (JCPDS PDF no. 71-2494). In addition to that, few smaller peaks were also observed indicating the presence of $Bi_2Fe_4O_9$ (JCPDS PDF no 74-1098) and $Bi_{25}FeO_{40,}$ (JCPDS PDF no. 46-0416), which agrees with the reported literature [246, 247]. In N-rGO pattern, a characteristic peak (002) appeared at $2\theta = 26.11^0$. This indicates

a higher value shift of 2θ as compared to reduced graphene oxide due to the smaller atomic radius of nitrogen as compared to carbon, which confirms replacement of carbon atom with nitrogen in graphitic structure.

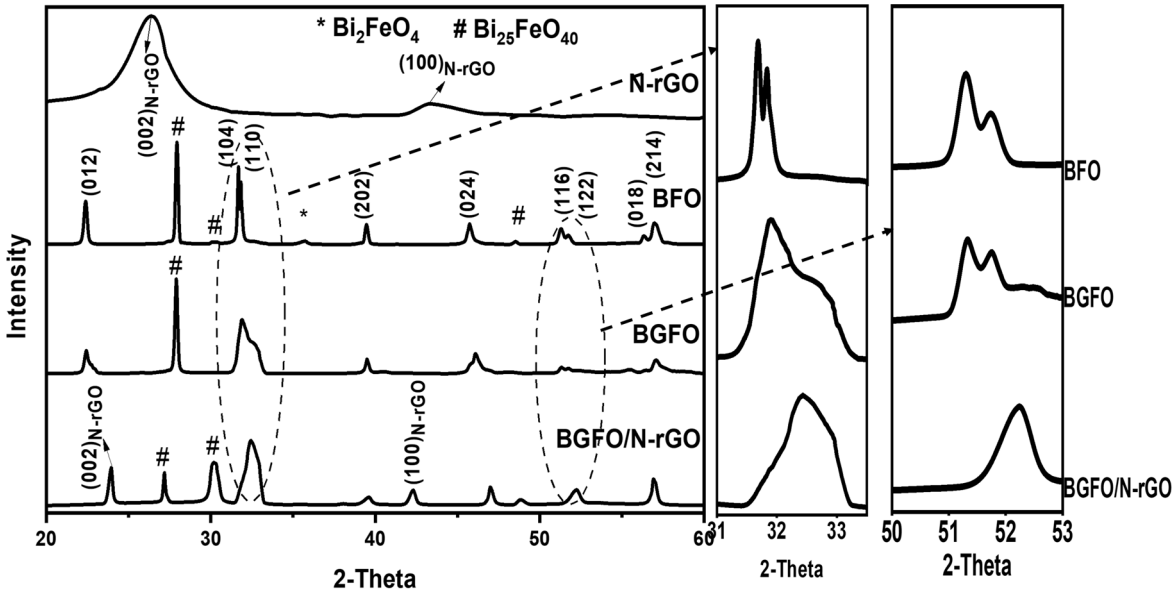

Fig. 4.2. 1 XRD patterns of N-rGO, BFO, BGFO and BGFO/N-rGO (enlarge sections around at 2-theta of 31 and 51 degree).

Two striking aspects were observed from Fig. 4.2.1 (enlarged section), firstly, characteristic peaks (104) and (110) of rhombohedral structured BFO overlapped and shifted toward higher 2-theta value, suggesting a structural phase transformation. The phase transformation from rhombohedral to orthorhombic resulted due to substitution of Gd^{+3} in place of Bi^{+3} ions [245]. Secondly, in BGFO/N-rGO the peaks corresponding to planes (116) and (122) get merged into a single peak as shown in magnified XRD pattern (in the range of 2θ between 51-53^0) which indicates chemical interaction of N-rGO with BGFO. A similar pattern was reported by Dixit et al., [248].

4.2.2 FTIR studies

FT-IR spectra were analyzed to investigate the vibrational frequencies in the catalysts, and bands are reported in Table 4.2.1. The band at 1462 and 1510 cm^{-1} attributed C-N bond (asymmetric vibration) and N-H bond (Fig. 4.2.2), respectively. The band at 1527 is assigned to C=C bond of sp^2 hybridized carbon. It showes incorporation of nitrogen in the graphetic structure [249]. BGFO/N-rGO spectra were also exhibited C=C and C-N bond vibration frequency that ascribed the presence of N-rGO support in the catalyst. Transmittance spectra of all catalysts showed Bi-O, Fe-O, Fe-O-Fe, and Bi-Fe bond vibrations near to the bands 540, 550, 581, and 839 cm^{-1}, respectively. Recent reports by Paschuta et al., [216] and Voll et al., [250] have have reported similar observations. The band at 565 cm^{-1} is ascribed to Gd-O bond in the spectra of BGFO that confirmed successful replacement of Bi^{+3} by Gd^{+3}. An additional band near to 639 cm^{-1} associated with Fe-O bond was appeared in all catalysts due to the presence of $Bi_2Fe_4O_9$.

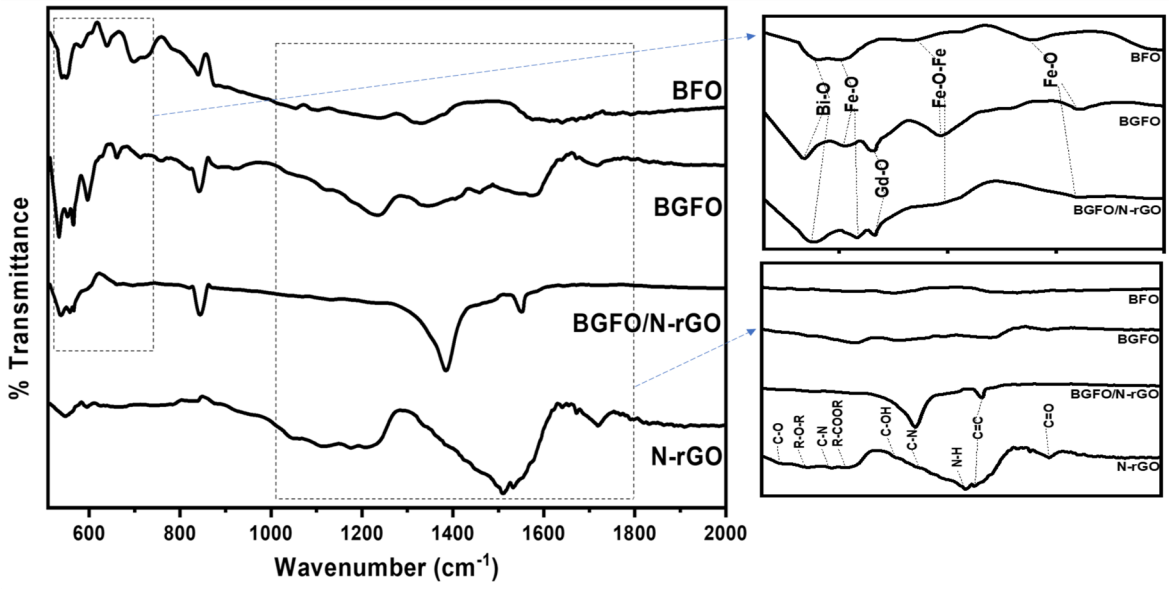

Fig. 4.2. 2 FTIR Spectra of BFO, BGFO, BGFO/N-rGO and N-rGO (enlarge sections between 510-700 cm^{-1} and 1000-1800 cm^{-1}).

Table 4.2. 1 Observed functional groups by FTIR Spectroscopy.

Functional groups	**Absorption peaks (cm^{-1}) in sample**			
	N-rGO	**BFO**	**BGFO**	**BGFO/N-rGO**
Bi-O strech in BiO_6	-----	540	533	538
Fe-O strech in FeO_6	-----	550	550	552
Gd-O	-----	-----	565	565
Fe-O-Fe bending	-----	581	596	596
Fe-O streching FeO_4	-----	639	659	660
Bi-Fe	-----	839	841	845
C-O epoxy group	1050	-----	-----	-----
R-O-R asymmetric strech in ether	1114	-----	-----	-----
C-N asymmetric streaching	1176	-----	-----	1176
R-COOR strech in ester	1209	-----	-----	-----
C-O-H bending in alcohol	1330	-----	-----	-----
C-N asymmetric vibration	1390	-----	-----	1384
C=C graphite	1534	-----	-----	1548
N-H deformation	1509	-----	-----	-----
C=O carbonyl group	1723	-----	-----	-----

4.2.3 Diffused reflectance spectroscopy (DRS) and photoluminescence studies

DRS absorbance spectra of BFO, BGFO, and BGFO/N rGO are shown in Fig 4.2.3 a. In BGFO/N-rGO, N-rGO was used as support, whereas BGFO and BFO were not supported. The absorption of BGFO/N-rGO was highest because of N-rGO due to the transition from $\pi \rightarrow \pi^*$ band (π band of C to π^* band of N) [251]. The band gap of the catalysts was calculated from Tauc's plots of $(\alpha h\vartheta)^2$ vs hv, as shown in Fig. 4.2.3b and the values are given in Table 4.2.2. BGFO/N-rGO exhibits the lowest bandgap in comparison to BGFO and BFO. The two major ways to decrease the bandgap of BFO are compositional change (chemical interaction) and charge transfer from oxygen to Fe ion [252]. Therefore, doping of Gd in BFO created a new electronic band (4f orbital of Gd) close to the lower edge of the CB. The photoinduced electrons can be transferred from O 2p to Gd 4f instead of the Fe 3d state that resulted in a significant reduction in the bandgap energy [253]. In BGFO/N-rGO composite, hybridization of C 2p orbitals (N-rGO) with valance band and conduction band (BGFO) introduced a new energy state near fermi level of BGFO. Therefore, the bandgap of BGFO decreased after interaction with the support (N-rGO) [222].

Fig. 4.2.3c shows fluorescence spectra of BFO, BGFO and BGFO/N-rGO. Photoluminescence (PL) emission depicts photoinduced electron-hole pair recombination ability [151]. All photocatalysts show a similar emission at 529 nm with different intensity. BGFO/N-rGO exhibited weakest PL intensity, which attributed the lowest rate of electron-hole pair recombination. This implies that photogenerated electrons quickly move from BGFO to N-rGO. Therefore, photoinduced electron-hole pair recombination was suppressed to a great extent leading to enhanced photocatalytic performance, and thus it is clear that the activity of catalysts followed the trend, i.e., BGFO/N-rGO> BGFO> BFO.

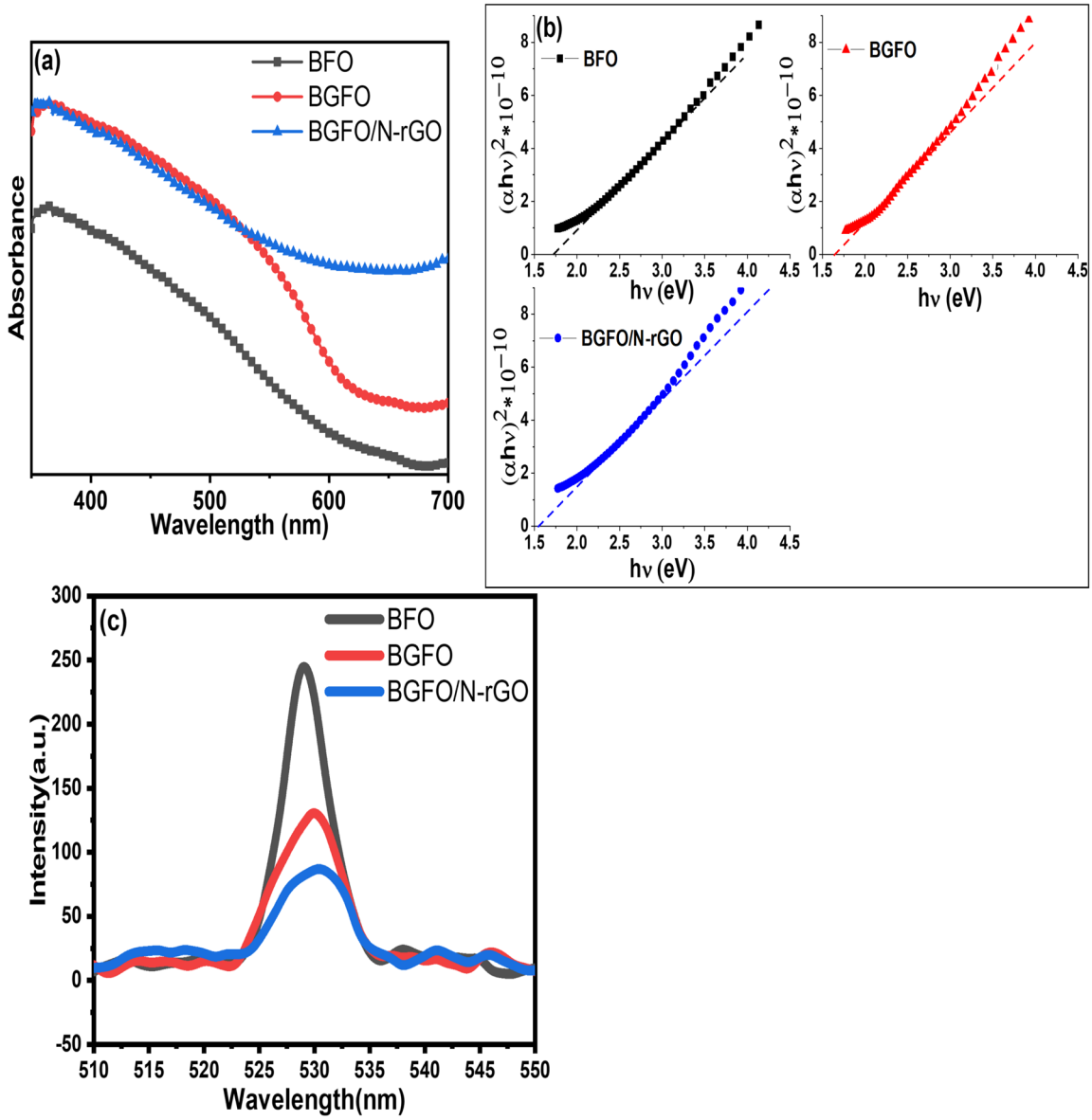

Fig. 4.2. 3 (a) DRS absorbance, (b) Tauc's Plot, (c) PL Spectra of BFO, BGFO and BGFO/N-rGO.

Table 4.2.2 Bandgap, surface area, average crystallite size and particle size of BFO, BGFO, and BGFO/N-rGO.

Catalyst	**Bandgap (eV)**	**Surface Area ($m^2 . g^{-1}$)**	**Average Crystallite size from XRD (nm)**	**Particle size from TEM (nm)**
BFO	1.72	1.4	44	47
BGFO	1.67	2.6	33	35
BGFO/N-rGO	1.56	22.1	35	36

4.2.4 Morphological analysis

Surface morphology of catalysts were analyzed by SEM and TEM, as shown in Fig. 4.2.4(a-f). The SEM image of BFO showed irregular particle size. Substitution of Gd in BFO (BGFO) exhibited smaller particle size as compared to BFO. Gd-doping induces two changes in pristine bismuth ferrite, namely, strain development and suppression of

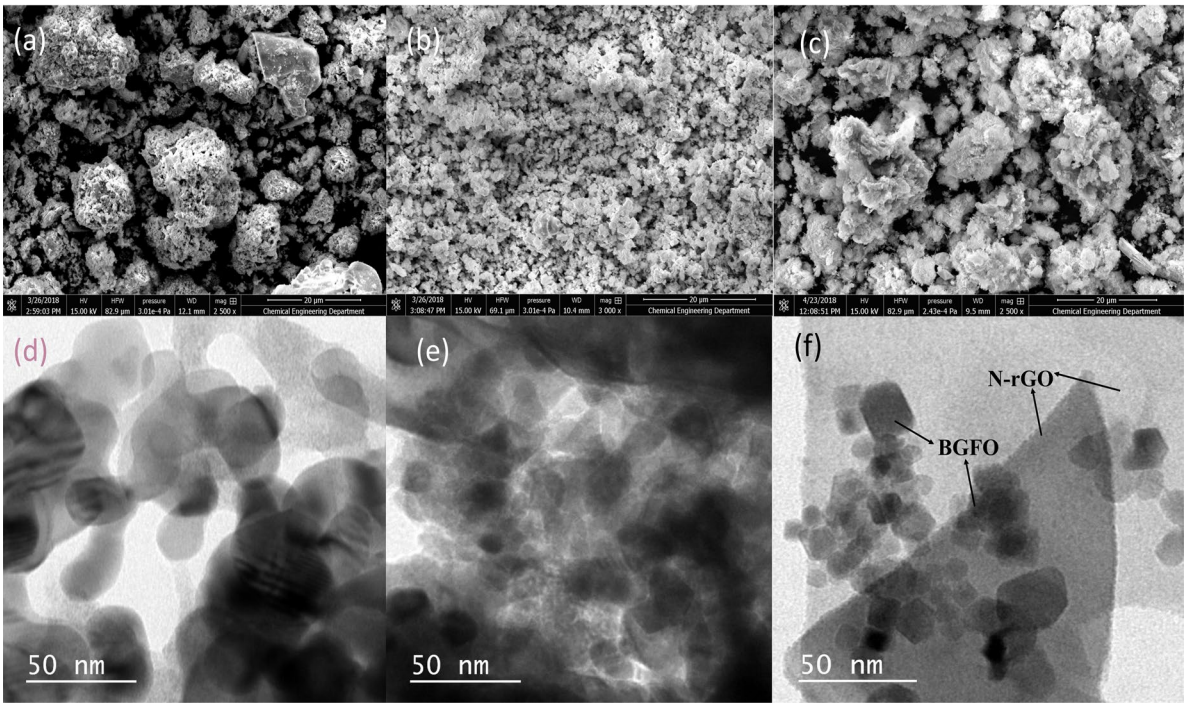

Fig. 4.2. 4 SEM image of (a) BFO, (b) BGFO, and (c) BGFO/N-rGO; TEM image of (d) BFO, (e) BGFO, and (f) BGFO/N-rGO.

Bi volatilization [254]. Strain development inhibited the grain growth leading to a decrease in particle size. Similarly, SEM image of BGFO/N-rGO also exhibited smaller particle size as compared to BFO. EDX analysis also confirmed the presence of the elements such as Bi, Gd, Fe, O, C, and N in the samples (Fig. 4.2.5). Further, microstructure of all the catalysts was investigated by TEM analysis, which depicted that

BGFO successfully segregated on the N-rGO surface (Fig. 4.2.4f). Average particle size was computed for all the catalysts and is tabulated in Table 4.2.2. The particle size of

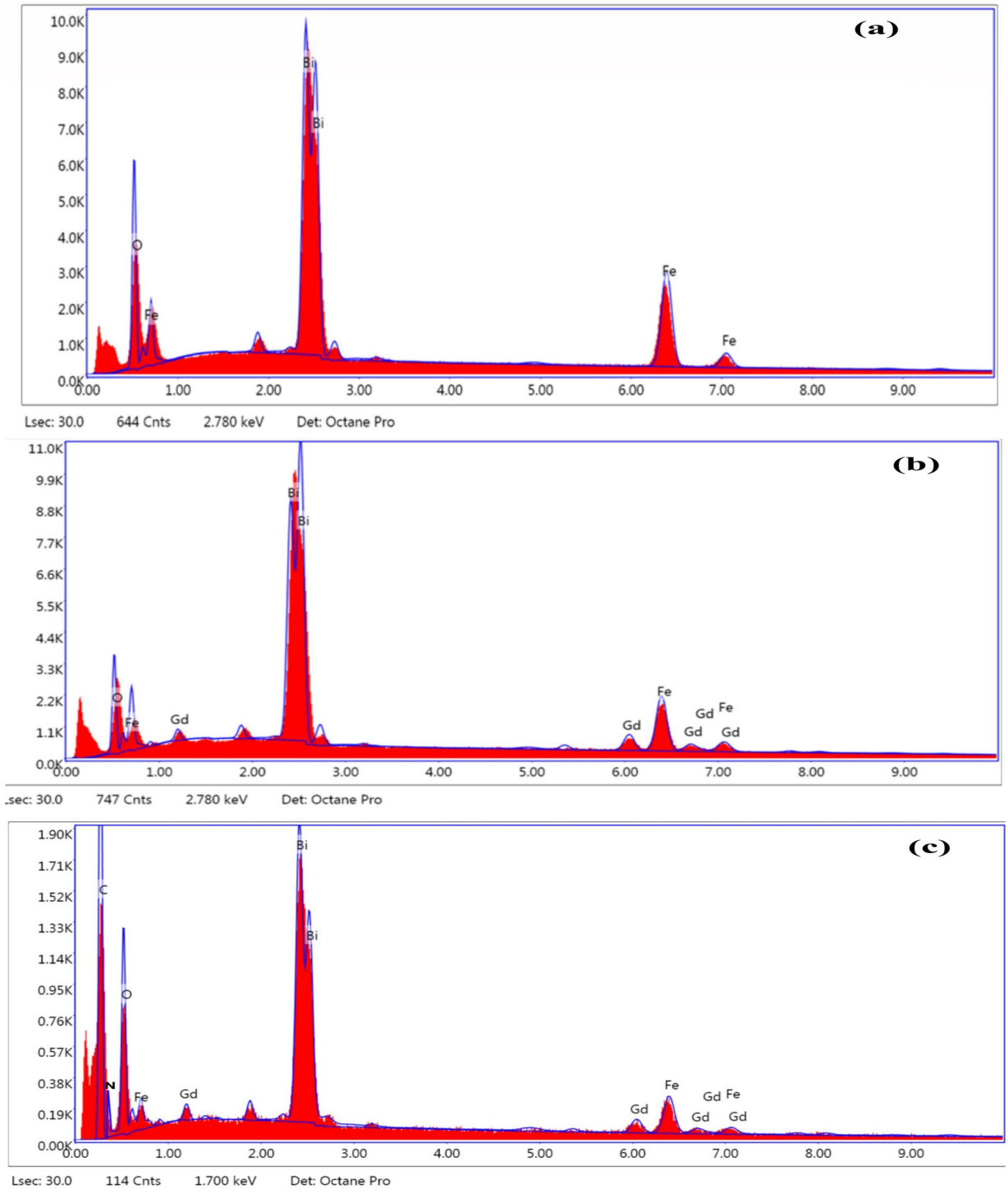

Fig. 4.2. 5 EDX of (a)BFO, (b)BGFO, and (c)BGFO/N-rGO.

BFO, calculated from TEM image (47 nm), established a strong agreement with particle size calculated from XRD results (44 nm). As expected, BGFO exhibited smaller particle size (35 nm) as compared with bismuth ferrite due to Gd substitution in place of Bi. BGFO/N-rGO also exhibited similar size as compared to BGFO that interpreted dispersion of BGFO on N-rGO surface.

4.2.5 XPS studies

Identification of elements and their chemical interactions on the surface of photocatalysts were examined by X-ray photoelectron spectroscopy (XPS). The survey spectra of the catalysts are given in Fig. 4.2.6. All peaks were deconvoluted with the help of Lorentzian-Gaussian method [255]. Fig. 4.2.7a exhibited N1s peak (deconvoluted) of N-rGO into

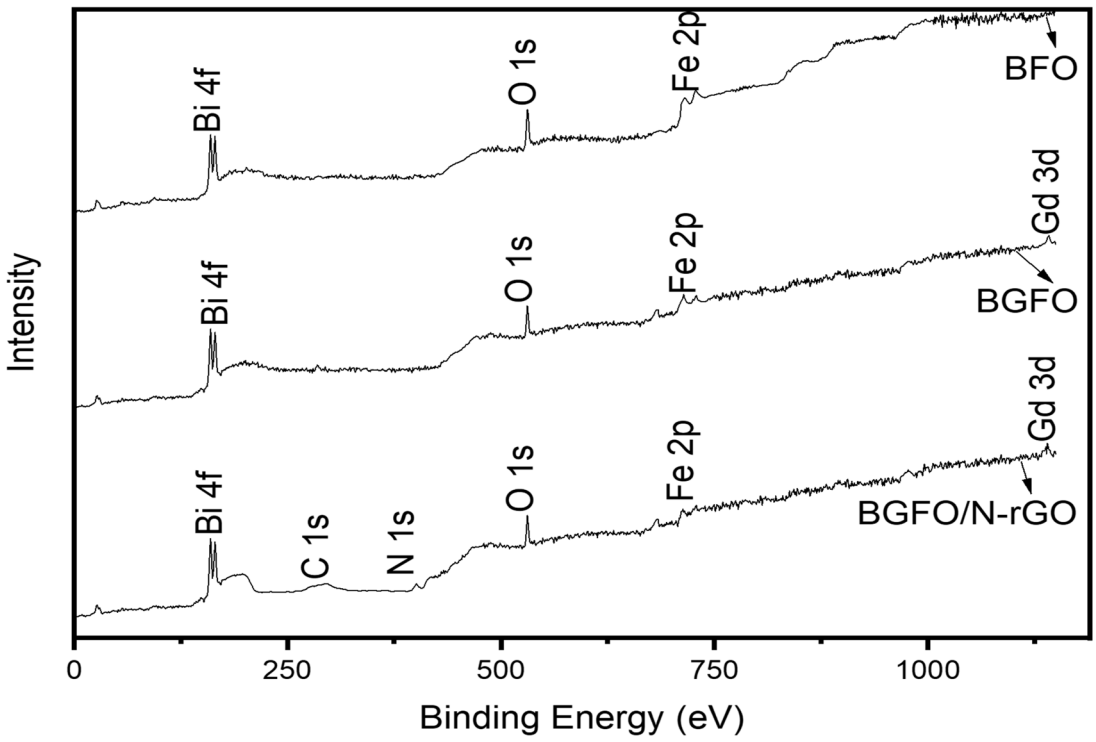

Fig. 4.2.6 Survey spectra of BFO, BGFO, and BGFO/N-rGO.

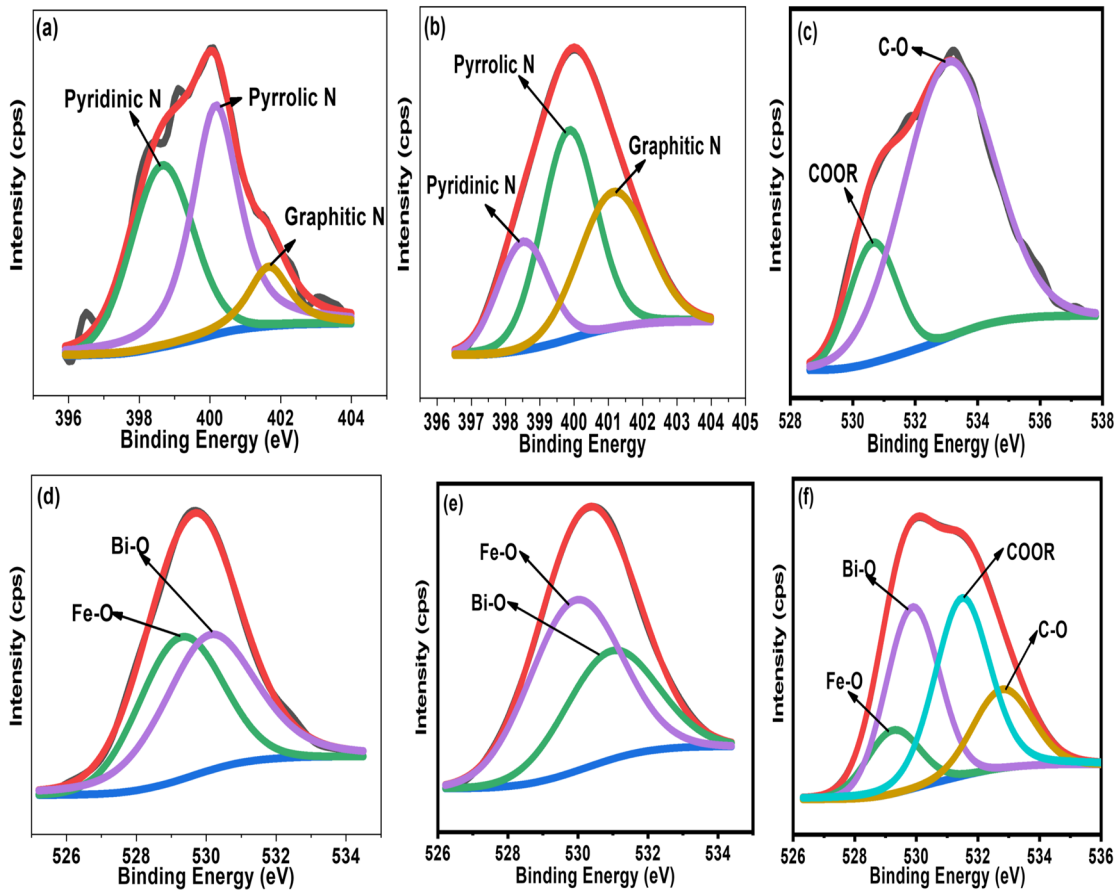

Fig. 4.2. 7 XPS spectra of N1s in (a) NrGO (b) BGFO/N-rGO; XPS spectra of O 1s in (c) NrGO (d) BFO (e) BGFO (f) BGFO/N-rGO.

three peaks viz. pyridinic (398.6 eV), pyrrolic (400.1 eV), and graphitic nitrogen (401.6 eV) confirming a successful doping of nitrogen into the graphene oxide [224, 256]. N 1s peak of BGFO/N-rGO (Fig. 4.2.7b) also exhibits these three peaks. The peaks' values are given in Table 4.2.3. Fig. 4.2.7(c-f) exhibited the deconvoluted spectra of O 1s for N-rGO, BFO, BGFO, and BGFO/N-rGO. Binding energies of deconvoluted O 1s peaks are given in Table 4.2.3. Two peaks were observed in N-rGO spectra centered at ~533 eV and ~530.6 eV assigned to C-O and C-OOR, respectively [224]. Deconvoluted peaks of O 1s in BFO, BGFO, and BGFO/N-rGO were centered at ~529.3 eV and ~530 eV

corresponding to Fe-O and Bi-O, respectively [226]. It is observed that binding energies of C-O and C-OOR shifted to a lower value in BGFO/N-rGO in comparison to N-rGO. This indicated occurrence of electronic redistribution leading to chemical interaction between support (N-rGO) and BGFO. The chemical interaction resulted into the formation of BGFO/N-rGO heterojunction, which provides a path for the transfer of electrons and suppresses photoinduced charge recombination [227].

Table 4.2.3 Binding energies of O1s and N 1s.

Sample	**B.E. (eV) of O 1s in different bonds**				**B.E. (eV) of N 1s in different bonds**		
	Fe-O	**Bi-O**	**C-OOR**	**C-O**	Pyridinic-N	Pyrrolic-N	Graphitic-N
N-rGO			531.7	533.0	398.6	400.1	401.6
BFO	529.3	530.1	-----	-----	-----	-----	-----
BGFO	529.3	530.1	-----	-----	-----	-----	-----
BGFO/N-rGO	529.2	529.9	531.5	532.8	398.6	400.1	401.6

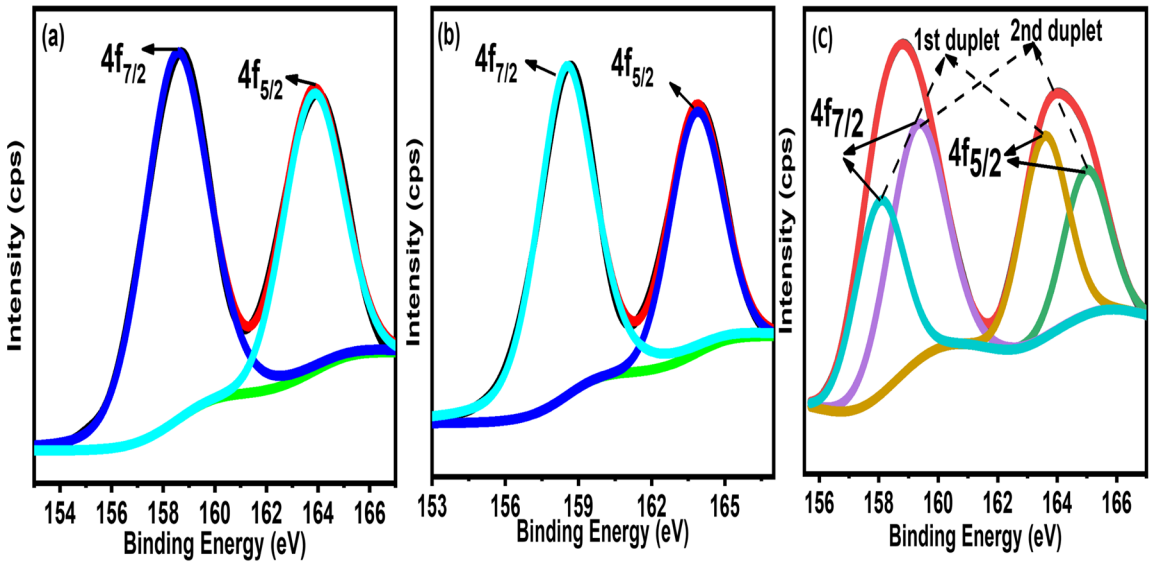

Fig. 4.2. 8 XPS spectra of Bi 4f in (a) BFO (b) BGFO (c) BGFO/N-rGO.

XPS spectra of Bi 4f of the photocatalysts showed peaks centered at 158.2 eV and 163.5 eV (Fig. 4.2.8(a-c)) attributed to Bi 4f in BFO and separation between spin-orbit around 5.3 eV which confirms the existence of bismuth in the form of Bi^{+3} state [257]. In the case of BGFO/N-rGO, two doublets were observed. The first doublet is assigned at binding energies of 158.2 eV and 163.5 eV, and second doublet is assigned at binding energies of 160.3 eV and 165.8 eV. The first doublet was ascribed to Bi^{+3} in Bi-O bond, and the second doublet was attributed to Bi^{+3} in Bi-O-C bond. The binding energies of Bi 4f were shifted to higher binding energy due to decrease in electron density. This is due to the higher electronegativity value of carbon and oxygen with comparison to bismuth [229]. Hence, this result confirms formation of heterojunction between N-rGO and BGFO by formation of Bi-O-C bond. Fig 4.2.9 (a and b) shows core level Gd $3d_{5/2}$ and $3d_{3/2}$ states at ~1189.6 and ~1221.4 eV, respectively, revealed the oxidation state of Gd^{+3} [336].

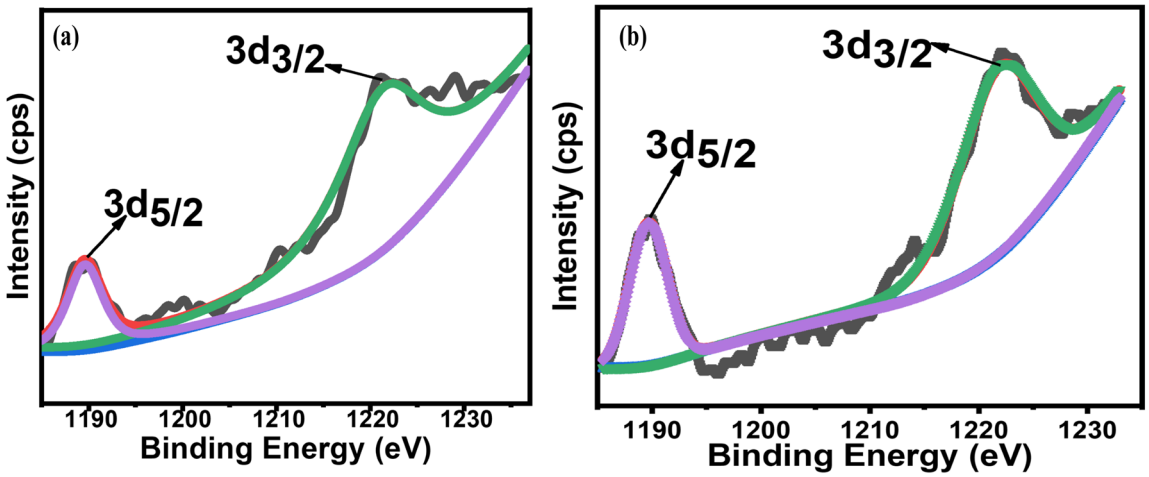

Fig. 4.2. 9 XPS spectra of Gd 3d in (a) BGFO, (b) BGFO/N-rGO.

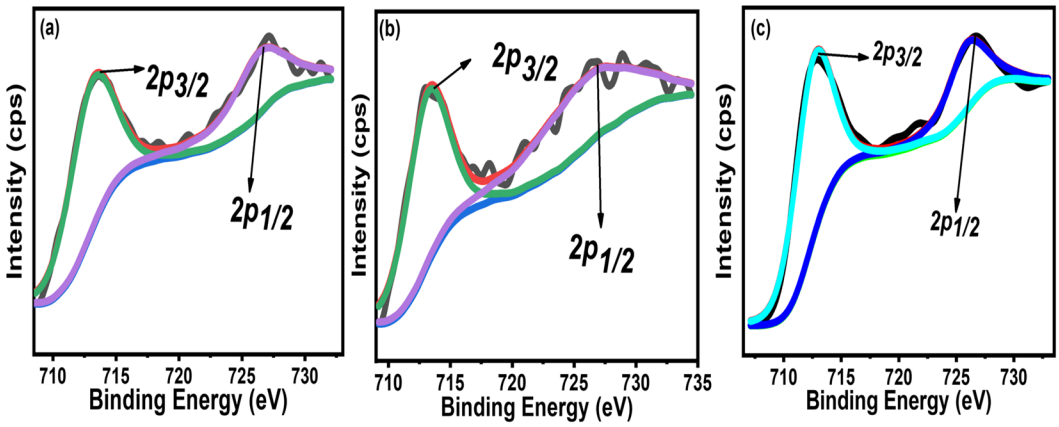

Fig. 4.2.10 XPS spectra of Fe 2p in (a) BFO, (b) BGFO, and (c) BGFO/N-rGO.

Fig. 4.2.10 shows two peaks of Fe 2p at 710.8 eV and 723.8 eV, which correspond to Fe $2p_{3/2}$ and Fe $2p_{1/2}$ peaks, respectively. The difference between Fe $2p_{3/2}$ and satellite peak (718.8 eV) was found 8 eV that confirmed existence of Fe^{+3} in all catalysts [230]. All the binding energies of Bi^{+3}, $Fe^{+3,}$ and $Gd^{+3}$are given in Table 4.2.4. In photocatalyst

BGFO/N-rGO, a positive binding energy shift was observed only in Bi^{+3}, however, no change was observed in Fe^{+3} and Gd^{+3} spectra.

Table 4.2. 4 Binding energies of Bi 4f, Fe 2p and Gd 3d.

Sample	**B.E (eV) of Bi^{+3}**				**B.E (eV) of Fe^{+3}**		**B.E (eV) of Gd^{+3}**	
	First-Doublet(I)		**Second-Doublet(II)**					
	$4f_{7/2}$	$4f_{5/2}$	$4f_{7/2}$	$4f_{5/2}$	$2p_{3/2}$	$2p_{1/2}$	3d 5/2	3d 3/2
BFO	158.5	163.8	-----	-----	713.0	726.3	-----	-----
BGFO	158.9	164.8	-----	-----	714.3	726.7	1189.6	1221.4
BGFO/N-rGO	158.1	163.6	159.3	165.0	713.5	726.6	1189.6	1221.4

4.2.6 BET surface area analysis

Nitrogen adsorption-desorption curves of BFO, BGFO and BGFO/N-rGO are given in Fig. 4.2.11 and all the sample exhibited type-IV isotherm, indicating the mesoporous structure. The BET surface areas of BFO, BGFO, and BGFO/N-rGO were calculated from N_2 adsorption and tabulated in Table 2. Surface area of BGFO/N-rGO (22.1 m^2g^{-1}) was observed sixteen-folds higher than that of BFO (1.4 m^2g^{-1}). This indicates the significant contribution of N-rGO in achieving high surface area. This can facilitate more adsorption sites for more reactant molecules, which will enhance the photocatalytic activity.

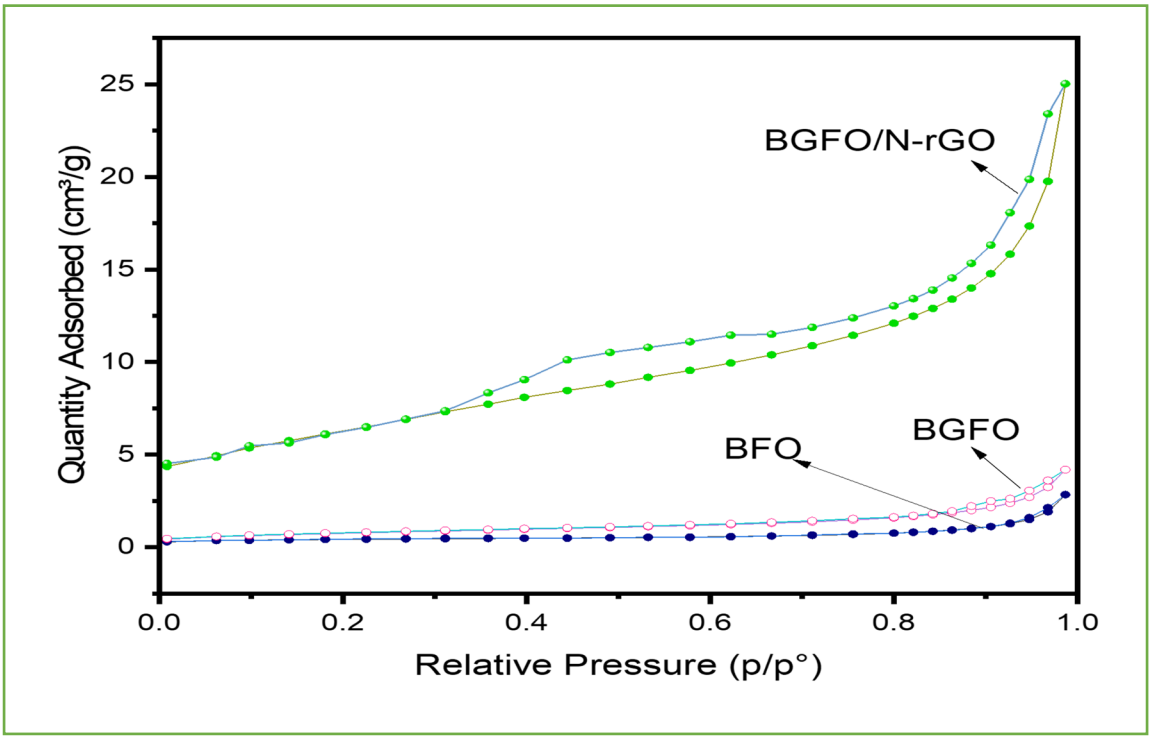

Fig. 4.2.11 Nitrogen adsorption- desorption isotherm of BFO, BGFO and BGFO/N-rGO.

4.2.7 Electrochemical impedance spectroscopy and Mott-Schottky analysis

Charge transfer resistance for the catalysts was analyzed by electrochemical impedance spectroscopy (EIS) [258]. Interfacial charge transfer resistance can be analyzed by arc radius of the Nyquist plots (-imaginary impedance vs real impedance). Nyquist plot of BGFO/N-rGO (Fig. 4.2.12 a) exhibited the smallest arc radius amongst all the photocatalysts. The smallest arc radius attributed lowest charge transfer resistance leading to efficient charge transfer at the solid/liquid interface during photocatalytic process [259]. Charge carrier density and flat band potential were computed by Mott-Schottky (M-S) plots of the catalysts (Fig. 4.2.12 b). It was calculated by using Eq. 4.2.1 [232] and given in Table 4.2.5.

$$\frac{1}{C^2} = \frac{2}{\in_0 \in_r eN_D A^2}\left(V - V_{fb} - \frac{KT}{q}\right) \quad (4.2.1)$$

Where, *C, K, N_D, A, T, e, ε_0, ε, V_{fb}* and *V* denote observed capacitance, Boltzmann's constant, charge carrier density, surface area of the electrode, absolute temperature, electron charge, permittivity of the vacuum (8.854×10^{-12} Fm^{-1}), dielectric constant of BFO (~65), flat band potential, and applied potential, respectively [105]. Observed capacitance (C) of the catalysts was measured at a constant frequency (1.0 kHz) and applied potential was varied from 0.0 to 1.0 V. N_D and V_{fb} were estimated from the M-S plot, and positive slope of straight portion of the curve attributed p-type semiconductor [204]. BGFO/N-rGO showed the highest charge carrier density and flat band potential in comparison to BFO and BGFO. High flat band potential (0.91 V) of BGFO/N-rGO resulted in adequate band bending, causing an efficient charge separation, and high charge carrier density (1.01×10^{28} cm^{-3}) depicted a chemical interaction between solid/solid interface between BGFO and N-rGO. An electric field was developed in the graphitic skeletons of N-rGO due to the presence of nitrogen, leading to a polarized graphene matrix [260]. The polarization in N-rGO promoted photoinduced electron transfer from BGFO to N-rGO and thus inhibited photogenerated electron-hole pair recombination. Therefore, a successful interaction (chemically) was observed between N-rGO and BGFO, facilitating efficient and quick charge transfer leading to enhanced photocatalytic performance of BGFO/N-rGO.

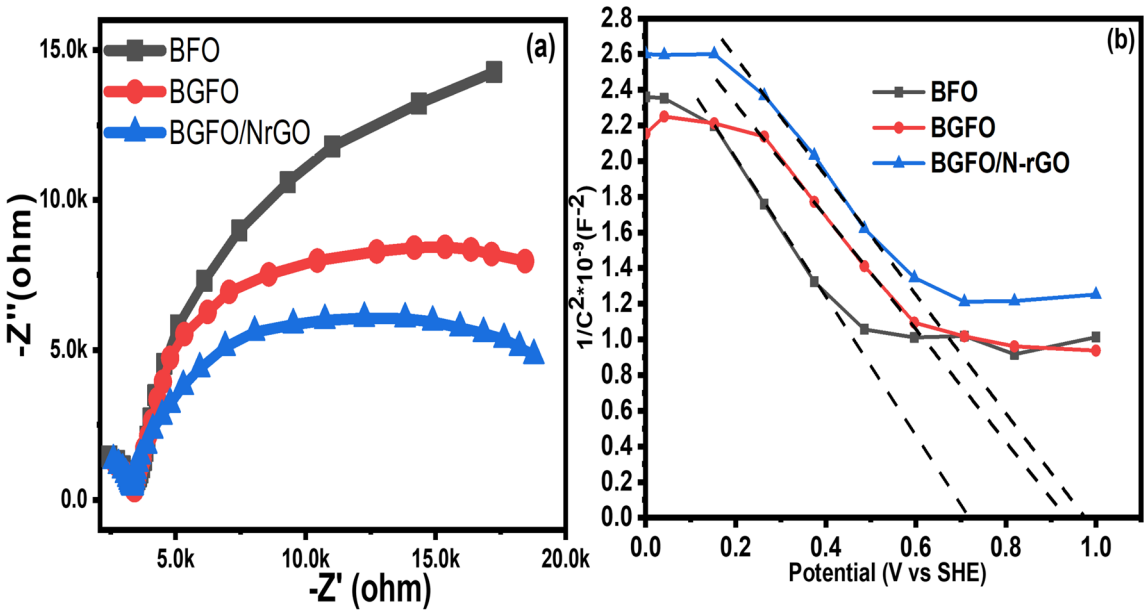

Fig. 4.2.12 Nyquist plots of BFO, BGFO, and BGFO/N-rGO; (b) Mott-Schottky Plots.

Table 4.2. 5 Flat band positions, carrier concentrations of BFO, BGFO, and BGFO/N-rGO.

Sample	**Flat band potential (V_{fb},V vs SHE)**	**Charge carrier density(N_D,cm^{-3})**
BFO	0.71	8.79×10^{27}
BGFO	0.91	8.82×10^{27}
BGFO/N-rGO	0.96	1.01×10^{28}

4.2.8 Photocatalytic performance

4.2.8.1 Activity and kinetic studies

Photocatalytic activities of BFO, BGFO, and BGFO/N-rGO were calculated through degradation of RhB dye, as shown in Fig. 4.2.13. The activity was measured in terms of

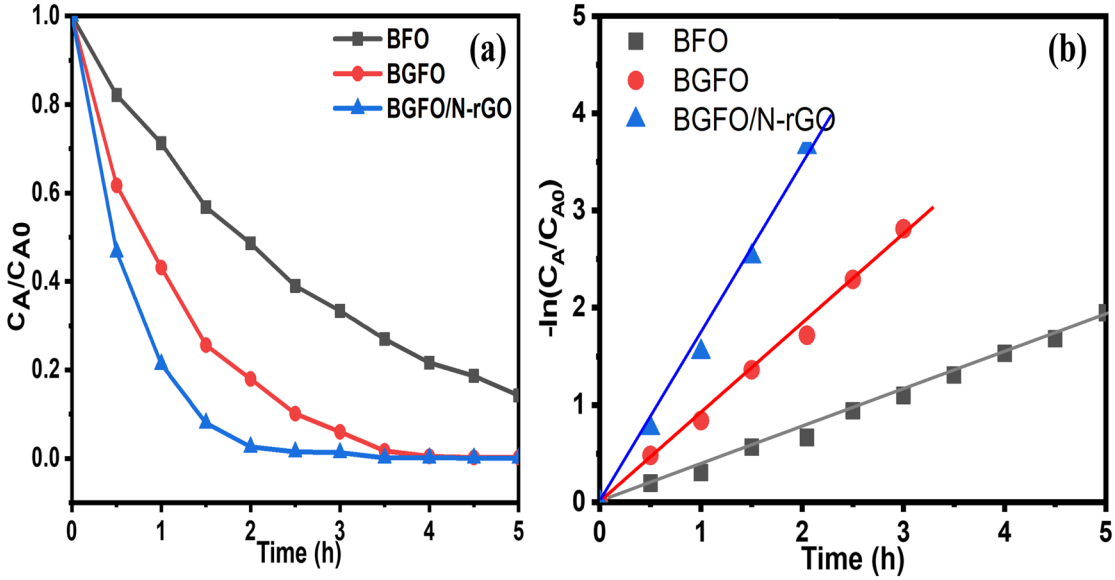

Fig. 4.2. 13 (a) Photocatalytic activity (Catalyst loading =120 mg.L-1, pH =4.3); (b) Reaction kinetics.

C_A/C_{A0} versus t, where t is the time (h), C_A is the concentration of RhB at t=t and C_{A0} is the initial concentration of RhB. initial 30 mg of catalyst was used in 250 mL RhB solution (C_{A0} = 10 mg/L). Preliminary studies showed that a very insignificant amount of the dye gets adsorbed on the surface of the photocatalyst in the dark. Therefore, the input concentration was taken as the initial concentration. Experiments were also carried out with light but without any photocatalyst. However, no change in the concentration of the dye with time was observed. It showed that the removal of dye was due to photocatalysis. Air was spurge through the solution of dye. Among all catalysts, BGFO/N-rGO showed the highest degradation of RhB (~99 % in 2 h) with the highest photocatalytic activity as compared to BGFO (98% in 3 h) and BFO (~92% in 5 h) (Fig. 4.2.13 a). Plot of $-\ln C_A/C_{A0}$ versus t showed a linear graph for all the catalysts, which confirms pseudo-first-order

kinetic (Fig 4.2.13 b). The slope of $-\ln C_A/C_{A0}$ versus t showed that BGFO/N-rGO exhibited the highest rate constant (18.91 $gcat^{-1}.h^{-1}$), which was 3-fold and 6-fold higher as compared to BFO and BGFO, respectively (Table 4.2.6). BGFO/N-rGO also exhibits better photocatalytic than BFO/N-rGO (RhB degraded 98.7% in 3 hr), as discussed in the section 4.1.9.6. Hence, BGFO/N-rGO showed best photocatalytic activity as compared with prepared catalysts.

Table 4.2.6 Rate constants of BFO, BGFO, and BGFO/N-rGO.

Sample	**Rate Constant (k, $gcat^{-1}.h^{-1}$)**
BFO	3.15
BGFO	7.89
BGFO/N-rGO	18.91

4.2.8.2 Effect of reactive species in degradation process and plausible mechanism

Trapping experiments were performed with BFO to understand the effect of active species in photocatalytic degradation process. In this process, superoxide radical ($O_2^{\cdot -}$) and hydroxyl radical ($OH^{\cdot}$) were generated with the help of photoinduced electron (e^-)-hole (h^+) pairs. It also takes part in degradation process. Hence, 1-4 benzoquinone (1-4 BQ), tert-butyl alcohol (TBA), potassium dichromate (PD) and ammonium oxalate (AO) were used as a scavenging agent for the radicals $O_2^{\cdot -}$, $OH^{\cdot}$, e^- and h^+, respectively [261-264]. Fig. 4.2.14 showed participation of all free radicals ($O_2^{\cdot -}$, $OH^{\cdot}$, e^- and h^+) in the degradation process. Addition of AO (1 mM) resulted in ~74% degradation in 5 h as compared to experiment performed in the absence of scavenger (~92% degradation in 5

h). However, the addition of TBA (1 mM) and PD (1 mM) showed degradation efficiency of 50.2% and 50.3%, respectively. Among all scavengers, addition of 1-4 BQ (1 mM) resulted in minimal degradation efficiency (44%), indicating the maximum participation of $O_2^{\cdot-}$ in the photocatalytic process. Moreover, addition of all scavengers simultaneously decreased the degradation efficiency up to 18%, which indicates collaborative participation of all reactive species in photocatalytic degradation experiment. Individual contribution of active species follows a trend in decreasing order as $O_2^{\cdot-} > OH^{\cdot} \approx e^- > h^+$. Among all reactive species, superoxide radical played vital role in photocatalytic process.

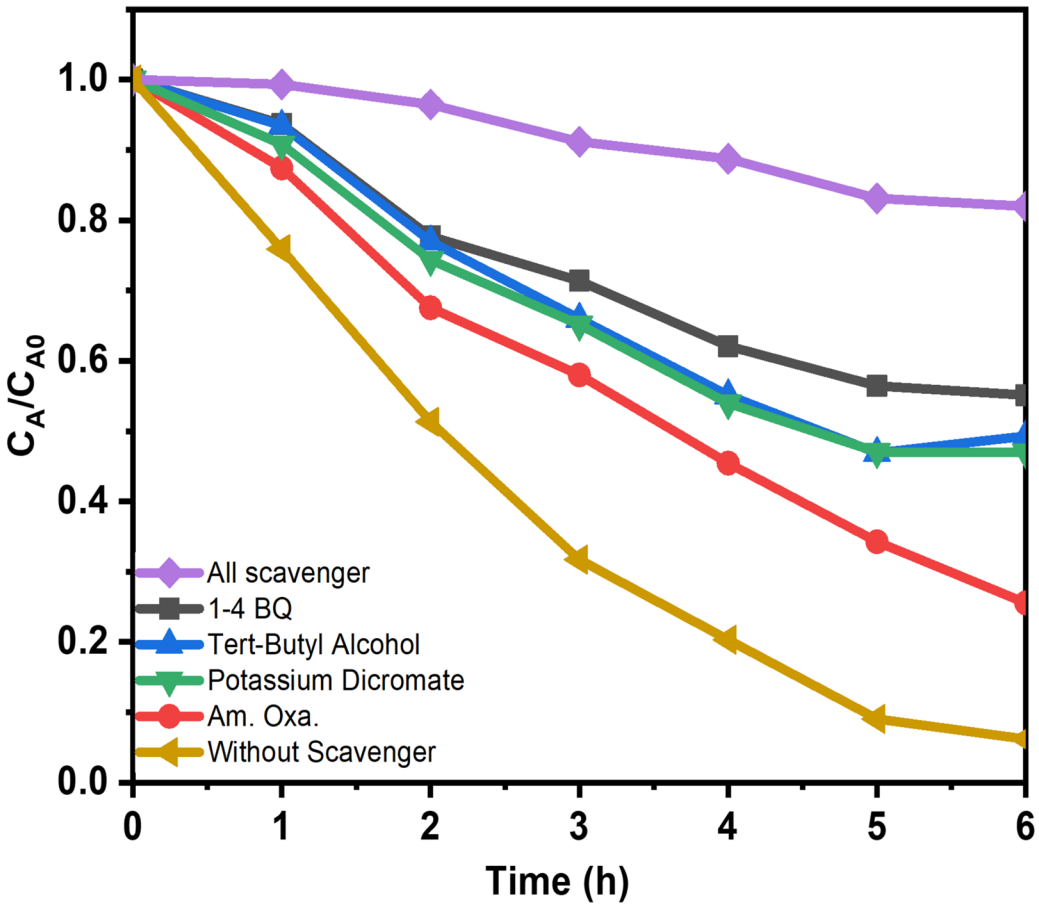

Fig. 4.2. 14 Reactive traping experiment for photocatalytic degradation of RhB.

Proposed reaction mechanism for the photocatalytic degradation process is shown in Fig. 4.2.15. In the presence of light, electrons are excited from valance band to the

conduction band of BFO (Eq. 2). In general, most of photoinduced electron-hole pairs recombine inside the catalyst. When Gd is used as a dopant in BFO, namely BGFO, it captures the excited electron immediately before the recombination process (Eq. 4). The captured electrons are transferred to the surface of the catalyst and react with oxygen to produce $O_2^{-\cdot}$ (oxidation potential -0.33 V Vs. NHE) [344]. Along with, photogenerated hole react with OH^- (from H_2O) to produce $OH^\cdot$ radical (oxidation potential +2.7 V Vs. NHE) [265]. Further, incorporation of N-rGO with BGFO forms a heterojunction between them, which suppresses photogenerated electron-hole pair recombination to a great extent. N-rGO also facilitates low charge transfer resistance at the solid-liquid interface in the heterojunction BGFO/N-rGO. All the possible reactions are given below.

$$BFO + hv \rightarrow BFO(e^- + h^+) \quad (4.2.2)$$

$$BGFO + hv \rightarrow BGFO(e^- + h^+) \quad (4.2.3)$$

$$Gd\ dopant + e^- \rightarrow e^-\ (Gd\ dopant\ trapped) \quad (4.2.4)$$

$$NrGO + e^- \rightarrow NrGO(e^-) \quad (4.2.5)$$

$$e^-\ (Gd\ dopant\ trapped)\ + O_2 \rightarrow O_2^{-\cdot} + Gd\ dopant \quad (4.2.6)$$

$$NrGO(e^-) + O_2 \rightarrow O_2^{-\cdot} + NrGO \quad (4.2.7)$$

$$BFO/BGFO(h^+) + OH^- \rightarrow BFO/BGFO + OH^\cdot \quad (4.2.8)$$

$$OH^\cdot + RhB \rightarrow H_2O + CO_2 \quad (4.2.9)$$

$$O_2^{-\cdot} + RhB \rightarrow H_2O + CO_2 \quad (4.2.10)$$

$$BFO/BGFO(h^+) + RhB \rightarrow H_2O + CO_2 \quad (4.2.11)$$

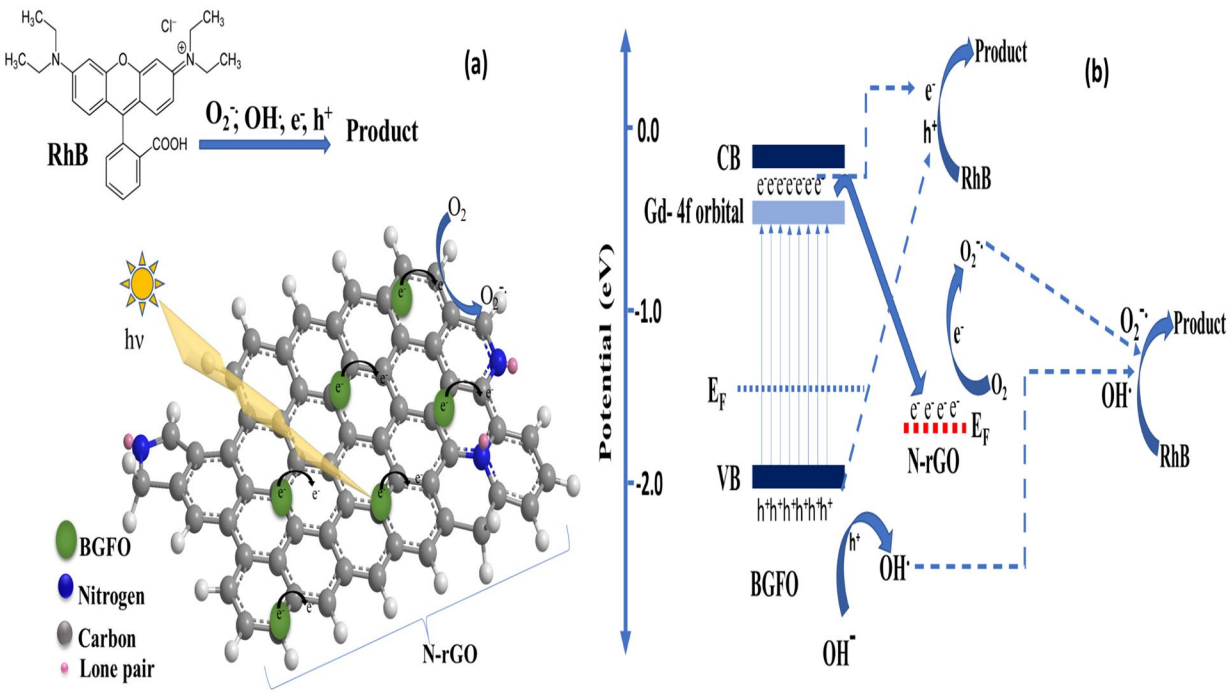

Fig. 4.2. 15 (a) Schematic illustration of photocatalytic degradation of RhB; (b)Magnified illustration of multiple charge transfer occurring in photocatalytic process.

4.2.9 Stability of the catalyst

Catalyst stability is one of the most important parameters for industrial use. Catalyst (BGFO/N-rGO) recovery efficiency of 99% was observed after five consecutive cycles of RhB degradation (10 ppm initial concentration). It was performed using the process, as mention in section 3.1. Fig. 4.2.16a shows the results of photocatalytic degradation of RhB with BGFO/N-rGO. No distinct change of activity was observed after five successive experiments. XRD patterns (Fig. 4.2.16b) of the catalyst before and after the photocatalytic reaction were found similar, which clearly indicates that the BGFO/N-rGO is a highly stable photocatalyst.

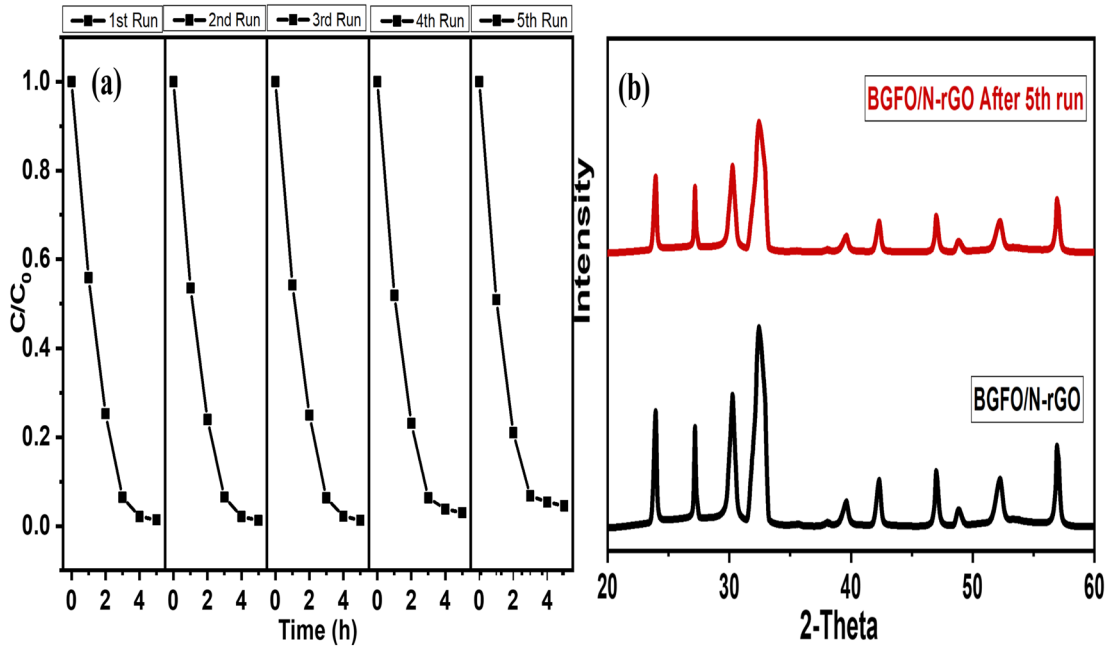

Fig. 4.2. 16 (a)The reusability of BGFO/N-rGO composite, (b)XRD spectra of BGFO/N-rGO before and after experiment.

4.2.10 Summary

BGFO/N-rGO showed enhanced photocatalytic activity due to the synergistic effect of mainly two factors; photoinduced electron-hole pair separation and charge transfer resistance. Photoinduced electron-hole pair separation was successfully achieved by substitution of Gd in place of Bi that was confirmed by XRD and XPS. It also restricted grain growth, which was observed in SEM imaging leading to better photocatalytic activity. Formation of the bond between bismuth of BGFO and carbon of N-rGO, lead to high charge mobility, which was confirmed by DRS and XPS. A rapid transformation of electrons from BGFO to N-doped reduced graphene was observed due to the reduction in the charge transfer resistance and high electron mobility of N-rGO. This resulted in the

suppression of the recombination of electron-hole pair as confirmed by EIS and PL. The support N-rGO increased the surface area of BGFO/N-rGO by 16 folds as compared with BFO leading to better adsorption of RhB. A synergistic effect of reduced photoinduced charge recombination, high charge mobility at the solid/solid interface of heterojunction, and high surface area resulted in the sufficient availability of electrons at the surface of the catalyst. Also, BGFO/N-rGO displayed high stability with 99 % recovery efficiency, even after five cycles of experiments. Thus, BGFO/N-rGO, a highly efficient and stable photocatalyst, has a high potential in future environmental remediation.

4.3 Sono-photocatalytic degradation of Rhodamine B over N-rGO supported Gd-doped bismuth ferrite heterojunction.

Recently, ultrasound assisted processes among different AOPs have been shown remarkable place for wastewater treatment [266, 267]. Alone sonolytic degradation process can convert water pollutant into carbon dioxide and water. Ultrasound wave is used in this process that produce acoustic cavitation leading generation of active free radical $OH^{\bullet}$ to degrade pollutant [268]. However, sonolytic degradation process takes very long reaction time to accomplish complete mineralization of pollutants. Therefore, generally sonolytic process is used in combination with other AOPs leading an effective way for mineralisation of water pollutants [268]. Herein, in this section, synergistic effect of photocatalysis and sonolysis has been examined on degradation of RhB on BGFO/N-rGO.

4.3.1 Sono-photocatalytic performances

4.3.1.1 Effect of catalyst loading

Fig. 4.3.1 shows a comparative assessment of photocatalytic and sono-photocatalytic degradation of RhB on varying catalyst (BGFO/N-rGO) loading. It is clearly seen from that in photocatalytic degradation process, on increasing catalyst loading, degradation efficiency increases and beyond optimum value (120 mg. L^{-1}) it decreases. Below optimum value adsorption sites play important role in degradation process and beyond optimum value adsorption active sites are occupied leading to aggregation of catalyst; hence, activity decreases. A detail explanation is discussed in section 4.1.10.

In case of sono-photocatalysis, degradation efficiency increases up to 160 $mg.L^{-1}$ as compared to photocatalytic process. In this process, segregation of photocatalyst achieve up to higher catalyst loading leading to enhanced degradation efficiency. Like photocatalytic process, beyond optimum catalyst loading, light scattering predominates

and photogenerated active species do not increase further leading to decreased degradation activity [187]. However, optimum value of catalyst loading is also depending on size, shape and reactor geometry. Therefore, optimization must be performed separately for each reactor configuration.

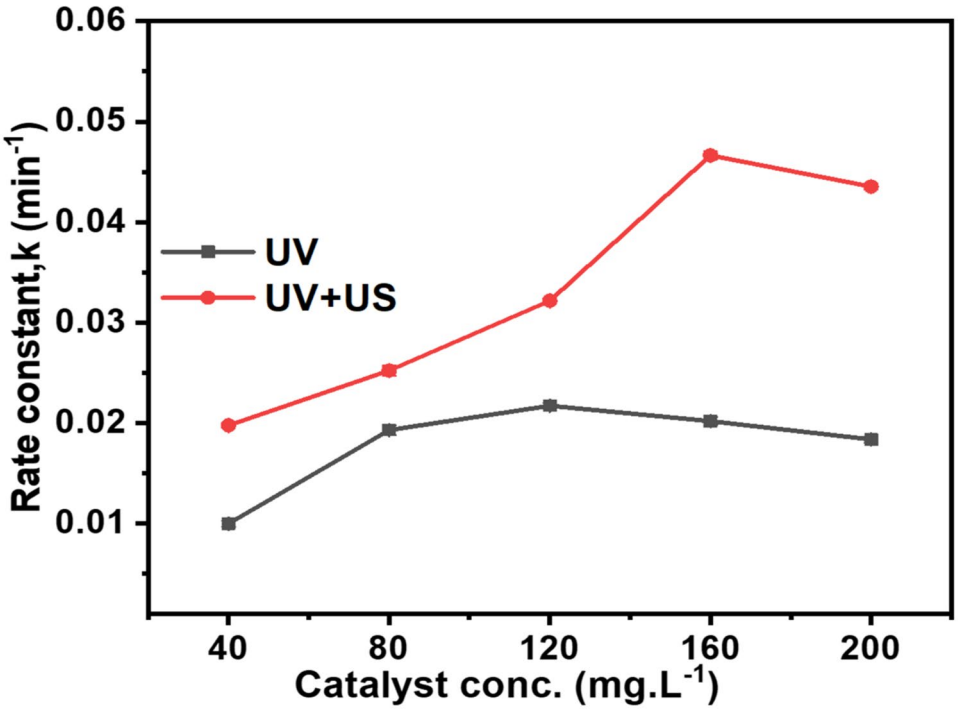

Fig. 4.3.1 Effect of catalyst loading.

4.3.1.2 Effect of dye concentration

The effect of initial concentration of RhB in the range of 5-30 ppm is investigated on its sono-photocatalytic degradation as shown in Fig. 4.3.2. Degradation efficiency of RhB solution increases from 5 to 20 ppm and decreases beyond 20 ppm. In photocatalytic system, as discussed in the section 4.1.10.2, degradation rate increases upto 10 ppm dye concentration while presence of ultrasonic wave (sonophotocatalytic process), the saturation active adsoption sites takes place at a relatively higher dye concentration. This can be explained that ultrasound interaction with catalyst produce the effect of microstreaming and also enhance mass transfer between solid/liquid interface leading to

regeneration of surface of catalyst. Hence, active adsorption sites become segregated [187, 188]. Further, the reaction can also take place at the cavitation bubble interface where the OH• concentration can reach a higher limit [269]. Therefore, the optimum value of RhB concentration is increased in sono-photocatalysis compared to photocatalysis.

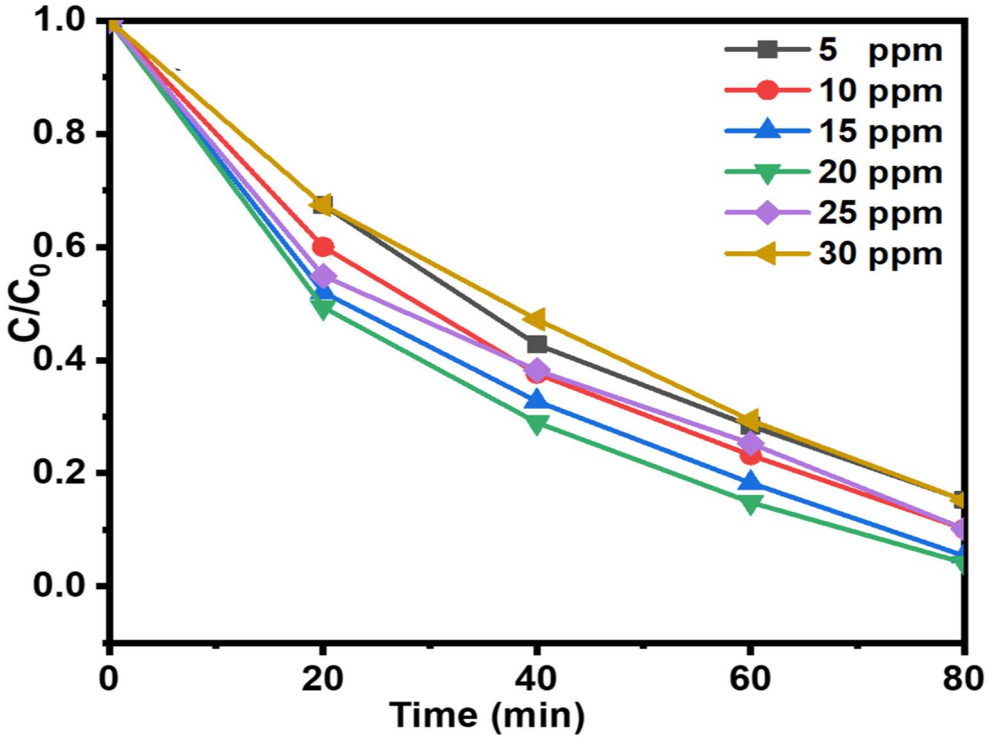

Fig. 4.3. 2 Effect of RhB concentration.

4.3.1.3 Effect of pH

Effect of pH on photocatalytic and sono-photocatalytic degradation of RhB is investigated in the range 2–10. The pH of the solution is maintained before light irradiation only. The results are presented in Fig. 4.3.3. Surface properties of catalyst mainly surface charge, size and shape are highly pH dependent [270]. In photocatalytic process, the degradation is more efficient in the acidic region than in the alkaline region

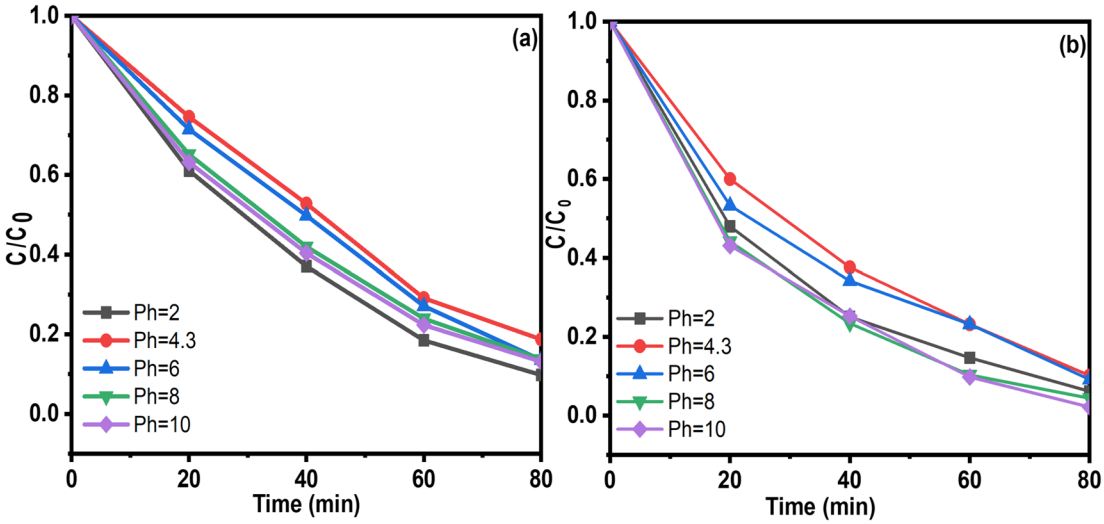

Fig. 4.3.3 Effect of pH on (a) Photocatalytic degradation; (b) Sono-photocatalytic degradation.

as shown in Fig. 4.3.3a and a detail explanation are discussed in section 4.1.10.3. However, in sono-photocatalytic process degradation efficiency increases in basic medium (Fig. 4.3.3b). As shown in Fig. 4.3.4, in pH range 2–6, the degradation rate of RhB under the photocatalytic and sono-photocatalytic process follows the same pattern, but sono-phocatalytic degradation showed a higher degradation rate in the simple medium after pH value 6 compared to the photocatalytic process. On changing pH value of the solution, various factors affect viz., substrate adsorption on the catalyst surface and formation of reactive species leading to change in degradation efficiency. Additionally, affecting the catalyst's surface properties, pH also affects direct RhB photolysis and $OH^{\bullet}$ radical generation [271]. The basic medium is predicted to promote the production of more $OH^{\bullet}$ radicals from the vast amount of OH^{-} ions present in the solution, which could increase degradation efficiency.

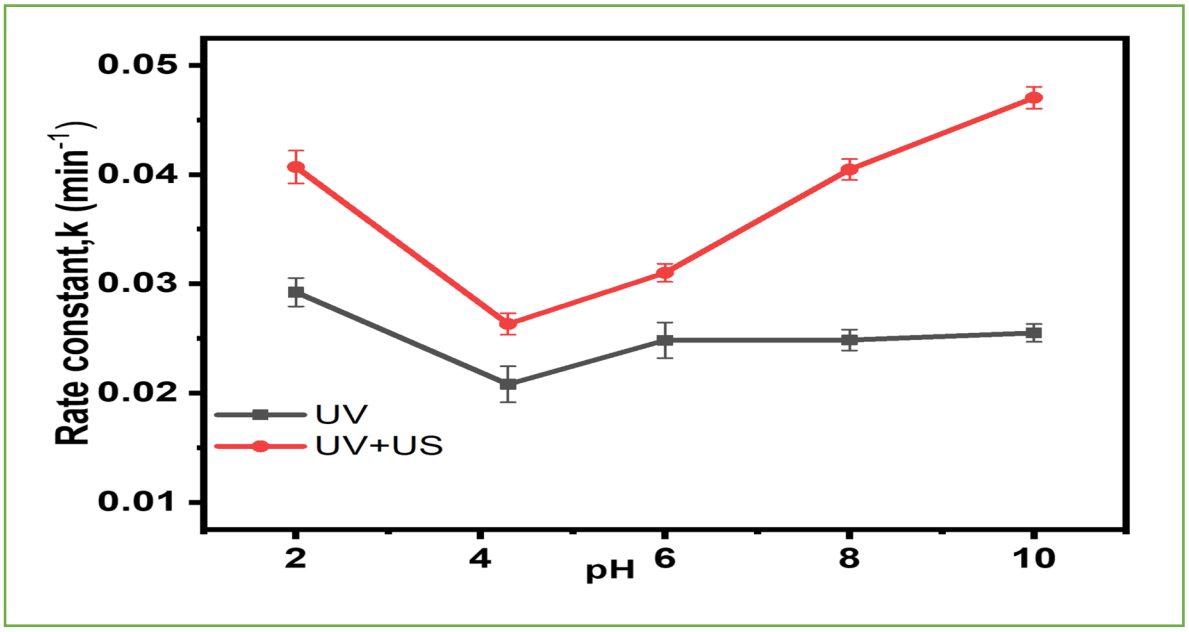

Fig. 4.3. 4 Comparative study of rate constant vs. pH between photocatalytic and sono-photocatalytic process.

4.3.1.4 Effect of ultrasonic power

Power density is one significant aspect affecting the efficiency of ultrasonic degradation. In this study, the influence of power density on the degradation of the RB solution (10 ppm) has been studied by varying it in the range of 5-40 KW. L^{-1}. Fig. 4.3.5 illustrates the influence of the density of power on the final RB concentration and it is clearly seen that with increasing acoustic power, the degradation efficiency increases, consistent with an increase in the development of $OH^{\bullet}$ radicals as described above. This can be explained that ultrasound power may boost degradation efficiency in terms of mainly: regenerating the catalyst surface due to microstreaming and mass transfer at solid/liquid interface increases due to shockwave propagation of wave [272, 273].

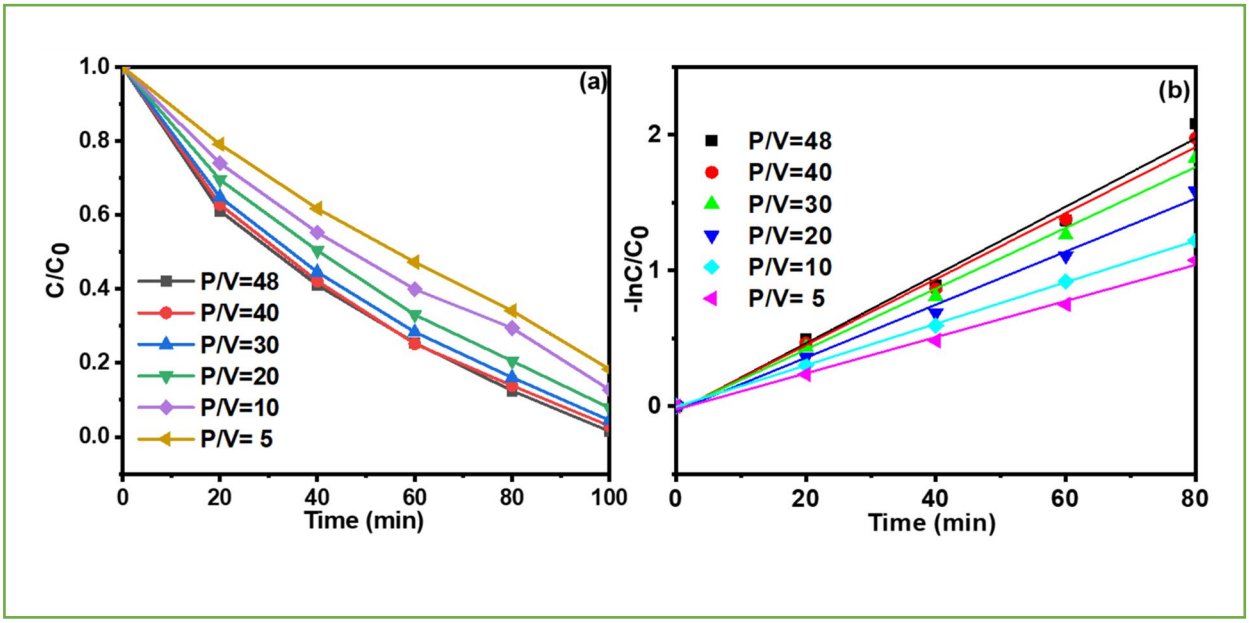

Fig. 4.3.5 (a)Effect of ultrasonic power density in sono-photocatalytic degradation of RhB. (b)Reaction kinetic plot.

4.3.1.5 Sonophotocatalytic activity

Preliminary investigations were carried out by using the BGFO/N-rGO catalyst under similar conditions for sonolytic, photocatalytic and sonophotocatalytic degradation of RhB. Experiments are conducted individually as well as in combination, in the absence of various factors such as catalyst, light and ultrasound, showed that either catalyst and light or catalyst and sound are required to affect degradation efficiency. As shown in Fig. 4.3.6, RhB degraded up to ~18% in 100 min by sonocatalytic process which is due mainly sonolysis of water leading to degradation of RhB. Water sonolysis generate free radicals $H^{\bullet}$ and $OH^{\bullet}$ as given in Eq. 4.3.1 [274].

$$H_2O \rightarrow H^{\bullet} + OH^{\bullet} \qquad (4.3.1)$$

Catalyst (BGFO/N-rGO) present into the solution create a heterogeneous system and it helps to breakdown microbubble into smaller pieces which is created by ultrasound. Therefore, number of microbubbles increases and high temperature and pressure induces inside the bubble due to cavitation process [275]. This increases the number of $OH^{\bullet}$

radicals, which interacts with the RhB present in the water and is oxidized, eventually leading to mineralization. The results show that the combination of light and sound (sonophotocatalysis) significantly improves RhB degradation in the presence of BGFO/N-rGO. Sonophotocatalysis resulted maximum degradation that is ~98.3% degradation in 100 min. However, in the case of photocatalysis, the degradation is ~93.5% after 100 min in comparison to sonolysis that is ~17.6%. According to the literature, ultrasound can increase degradation rate due to (a) the formation of active species (mainly $OH^{\bullet}$ and $OOH^{\bullet}$), (b) temperature rise and thus the acceleration of thermochemical reactions, (c) clean the catalyst surface avoiding the accumulation of contamination leading to enhanced light absorption and (d) improved transportation of intermediates at solid/liquid interface. Catalyst particle dispersion can increase the total surface area, provide more active sites for reactor adsorption, increase light absorption, and produce more reactive particles [191].

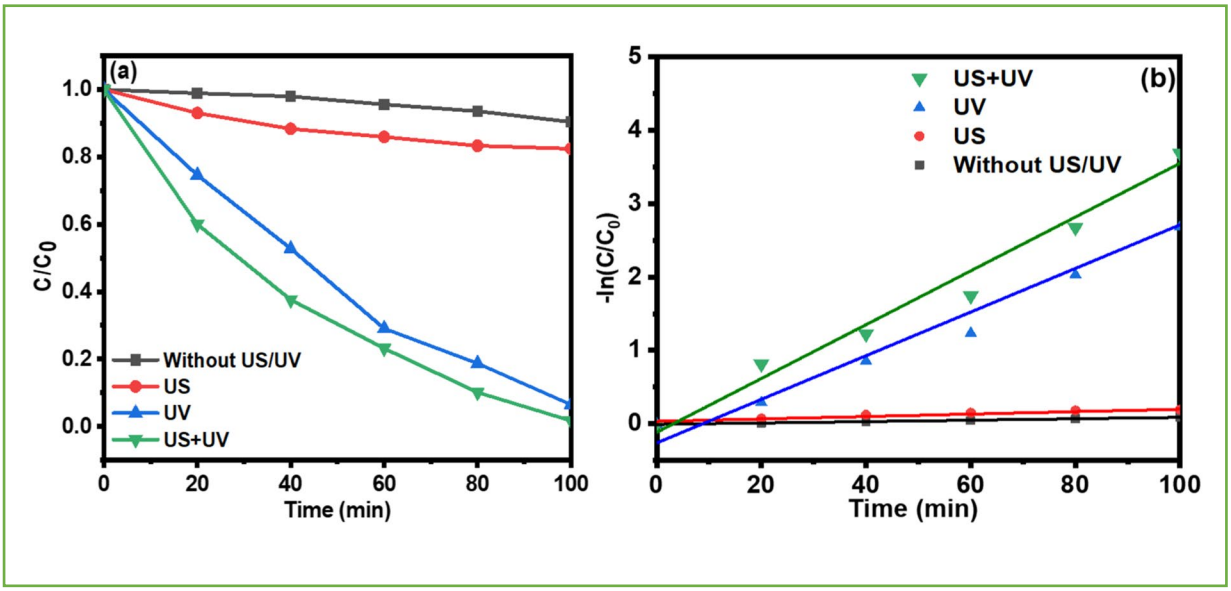

Fig. 4.3.6 (a) Sono-, photo- and sono-photocatalytic degradation of RhB and (b) corresponding rate constant.

Therefore, it is clear that RhB degradation under the influence of radiation (UV + US) is greater than the degree of decomposition during single UV and US irradiation,

thus exhibiting synergistic effects. The synergistic index of each process for degradation of RhB is calculated by using the Eq. 4.3.2 [276].

$$Synergy\ index = \frac{k_{US+UV}}{k_{UV} + k_{US}} \quad (4.3.2)$$

Where k_{US}, k_{UV} and k_{US+UV} are sono-, photo-, and sonophoto-catalytic degradation rates respectively. The values of rate constant and synergy index are calculated and given in Table 4.3.1.

Table 4.3.1 Rate constants and synergy index.

Process	**Rate constant (min^{-1})**	**Synergy index**
Without US/UV	0.00095	----------
US	0.00165	----------
UV	0.02172	----------
US+UV	0.04665	1.16831

4.3.1.6 Plausible mechanism of sono-photocatalytic degradation of RhB

Sonophotocatalytic degradation process is a combination of two advanced oxidation processes viz., sono and photocatalytic process as discussed in previous sections. A possible mechanism of sonophotocatalysis can be summarized as follows:

The photocatalytic degradation of RhB established to proceed as follows [363]:

Generation of UV-initiated electron–hole pairs

$$BGFO + hv \rightarrow BGFO(e^- + h^+) \quad (4.3.3)$$

Recombination of electron–hole pairs

$$h^+ + e^- \rightarrow heat \quad (4.3.4)$$

Formation of primary radicals by valence band holes

$$BGFO(h^+) + OH^- \rightarrow BGFO + OH^\bullet \quad (4.3.5)$$

$$BGFO(h^+) + H_2O \rightarrow H^+ + OH^\bullet \quad (4.3.6)$$

Scavenging of conduction band electrons

$$BGFO + e^- \rightarrow e^- (BGFO\ trapped) \quad (4.3.7)$$

$$NrGO + e^- \rightarrow NrGO(e^-) \quad (4.3.8)$$

Superoxide oxygen free radical formation

$$e^- (BGFO\ trapped) + O_2 \rightarrow O_2^{-\cdot} + BGFO \quad (4.3.9)$$

$$NrGO(e^-) + O_2 \rightarrow O_2^{-\cdot} + NrGO \quad (4.3.10)$$

$$RhB + Reactive\ species\ (O_2^{-\bullet}, OH^\bullet) \rightarrow Products \quad (4.3.11)$$

Water sonolysis is known that active radicals $OH^\bullet$ and $OOH^\bullet$ that attack organic compounds in solution are formed during by cavitation process [275]. The presence of BGFO/N-rGO particles enhances this phenomenon because the microbubbles tend to decompose into smaller ones, increasing the total number of high temperature and pressure regions [277, 278]. Further, cavitation produced by ultrasonication segregate catalyst particle and produce $OH^\bullet$ radical in aqueous phase leading to enhanced degradation rate. It also induces oxygen based free radical due to thermal decomposition

of dissolve oxygen in the aqueous solution. Due to cavitation possible reactions are given below:

$$H_2O \rightarrow H^{\bullet} + OH^{\bullet} \quad (4.3.14)$$

$$H^{\bullet} + OH^{\bullet} \rightarrow H_2O \quad (4.3.15)$$

$$H^{\bullet} + O_2 \rightarrow HOO^{\bullet} \quad (4.3.16)$$

$$O_2 \rightarrow 2O^{\bullet} \quad (4.3.17)$$

$$H_2O + O^{\bullet} \rightarrow 2OH^{\bullet} \quad (4.3.18)$$

$$OH^{\bullet} + OH^{\bullet} \rightarrow H_2O_2 \quad (4.3.19)$$

$$2OH^{\bullet} \rightarrow H_2O + O^{\bullet} \quad (4.3.20)$$

Most of the free radicals generated by cavitation process again combine inside the bubbles and form H_2O and O_2 (Eq. 4.3.21-4.3.23).

$$OH^{\bullet} + H^{\bullet} \rightarrow H_2O \quad (4.3.21)$$

$$O^{\bullet} + O^{\bullet} \rightarrow O_2 \quad (4.3.22)$$

$$OH^{\bullet} + HOO^{\bullet} \rightarrow O_2 + H_2O \quad (4.3.23)$$

The various active substances obtained as above react with RhB in bulk solution or at the gas/liquid interface of the bubble. The radicals namely $O^{\bullet}$, $HO^{\bullet}$ and HOO• can also transport to liquid/buble interface and may further transport into bulk solution leading to degradation of RhB (Eq. 4.3.24).

$$RhB + Reactive\ species\ (HOO^{\bullet}, O^{\bullet}, OH^{\bullet}) \rightarrow Products \quad (4.3.24)$$

4.3.2 Summary

In this study, sonophotocatalytic process is used to degrade RhB aqueous solution in the presence of BGFO/N-rGO catalyst. The combination of ultraviolet and ultrasound provides a synergy that significantly degraded the RhB solution. The optimum parameters are investigated for the degradation of RhB solution which are to be the initial concentration of 20 ppm RhB, 40 mg/l catalyst loading, power density of 40 KW. L^{-1}, and pH=10 within 80 min. Unlike the photocatalytic process, sonophotocatalytic exhibits the highest activity in the basic medium. However, the explanation is not clear due to the complexity of the combined process (sonolytic + photocatalytic). Sonophotocatalytic process improves the degradation efficiency of RhB, allowing complete degradation of the RhB in just 100 minutes, and increased kinetic rate constants by 28 and 2 times as compared to sonolytic and photocatalytic processes, respectively.